Composite Structures 320 (2023) 117041

Contents lists available at ScienceDirect

Composite Structures

journal homepage: www.elsevier.com/locate/compstruct

Stress-based topology optimization for fiber composites with improved stiffness and strength: Integrating anisotropic and isotropic materials

Rahul Dev Kundu [a], Xiaojia Shelly Zhang [a,b,c,*]

[a] Department of Civil and Environmental Engineering, University of Illinois Urbana-Champaign, 205 North Mathews Ave, Urbana, IL 61801, USA
[b] Department of Mechanical Science and Engineering, University of Illinois Urbana-Champaign, USA
[c] National Center for Supercomputing Applications, USA

ARTICLE INFO

Keywords:
Fiber-reinforced composite optimization
Multimaterial topology optimization
Stress constraint
Anisotropic yield criteria
Tsai–Wu criteria

ABSTRACT

Fiber-reinforced materials offer high stiffness- and strength-to-mass ratios to lightweight composite structures. To design stiff, strong, and lightweight fiber-reinforced composite structures, we propose a multimaterial anisotropic stress-constrained topology optimization framework that simultaneously optimizes geometry, distribution of anisotropic (i.e., orthotropic) and isotropic material phases, and local orientations of fiber reinforcements in the anisotropic phase. To achieve high performance in both stiffness and strength, we discover that both isotropic and anisotropic materials are needed: anisotropic materials are preferred in uniaxial members to increase stiffness, while isotropic materials are crucial at multi-axially stressed joints to enhance strength. We introduce multimaterial interpolation schemes to characterize both the stiffness and strength of composites made up of anisotropic and isotropic materials. The characterization of strength is enabled by a novel load factor-based yield function interpolation that consistently integrates anisotropic Tsai–Wu and isotropic von Mises yield criteria. We optimize stress-sensitive domains considering materials with various levels of stiffness and strength anisotropy as well as multiple load cases. The anisotropic stress constraints in the proposed framework effectively inform geometries to reduce stress concentration in fiber composites. The proposed framework provides a rational design paradigm for composite structures, capitalizing on dissimilar stiffness and strength properties of anisotropic and isotropic materials, to potentially benefit various engineering applications.

1. Introduction

Composites structures with anisotropic fiber reinforcements are widely used in aircraft design [1], construction [2], energy harvesting devices [3,4], soft robotics [5], soft actuation [6,7], and biomedical appliances [8]. Fiber-reinforced materials often have higher stiffness- and strength-to-mass [9] ratios along the fiber directions, enabling lightweight designs with significantly reduced material and cost. Such unique anisotropic properties can be further exploited using topology optimization [10–12] through improved material and fiber orientation distribution. Generally, topology optimization formulations for fiber-reinforced composites [13–23] are categorized into two fiber orientation approaches. The first approach varies the fiber orientations continuously within a permissible range [2,13,14,24–32] (e.g., from $\theta_{min} = -\pi/2$ to $\theta_{max} = \pi/2$), and the second approach chooses the best possible fiber distribution from a predefined set of discrete candidate orientations [19,33–36]. While the first approach with continuously varying fiber orientations has more design freedom, the second approach with discrete fiber orientations offers easier fabrication for many practical applications. Moreover, the second approach is suitable for multimaterial topology optimization that allows simultaneous consideration of multiple dissimilar materials. This study adopts the second approach to optimize composite structures considering both anisotropic fiber-reinforced and isotropic materials. For fiber-reinforced materials, we consider the orthotropic subclass of anisotropic materials to present the optimization framework and design examples in this work.

Design optimization of fiber-reinforced composites requires the incorporation of the anisotropic material strength information in some form, e.g., stress constraints, to prevent local material failure during operation. Yet, topology optimization considering strength anisotropy is rarely investigated. Anisotropic yield criteria, such as Tsai–Hill and Tsai–Wu, are mostly incorporated in laminate stacking optimization problems [37–40] which ignore in-plane variation of fiber orientation.

* Corresponding author at: Department of Civil and Environmental Engineering, University of Illinois Urbana-Champaign, 205 North Mathews Ave, Urbana, IL 61801, USA.
E-mail address: zhangxs@illinois.edu (X.S. Zhang).

https://doi.org/10.1016/j.compstruct.2023.117041
Received 23 August 2022; Received in revised form 27 March 2023; Accepted 15 April 2023
Available online 6 May 2023

A few laminate ply optimization studies [41–43] that optimize in-plane fiber orientation considering anisotropic failure criteria do not optimize the in-plane structural geometry, i.e., the spatial material occupancy. A similar limitation is observed in studies involving optimal fiber-reinforcement design for civil structures [2,44] (e.g., masonry and reinforced concrete), where the structural geometry is not concurrently optimized. A topology optimization work [45] incorporates anisotropic Tsai–Wu criteria focusing on manufacturing anisotropy in Fused Deposition Modelling (FDM) based 3D printing along and perpendicular to the build direction, which may not be suitable for fiber-reinforced composite topology optimization with multiple fiber orientations. Some recent studies optimize both geometry and in-plane fiber orientation with a single fiber-reinforced material considering anisotropic material strength, such as Tsai–Wu yield criteria [46] and Puck's failure criteria [47]. However, the overall strengths of such single-material fiber-reinforced composite structures are often limited by their weak anisotropic joints formed at the intersection of two or more uniaxial members. Using strongly anisotropic fiber-reinforced materials at the joints is inefficient because the joints usually have multi-axial load paths, and strong anisotropy arising from fiber reinforcement in any one direction is not always an optimal state [24,32].

Deviation of fiber alignment from any of the load paths disproportionately reduces the local material strength and stiffness along those load paths, both contributing to a significant boost in local stress. As a result, joints become considerably weak and prone to material failure compared to the uniaxial members, and the overall load-carrying capacity of the single-material fiber-reinforced composite structure decreases significantly. A feasible solution to address this weak joint problem is the utilization of material heterogeneity through multimaterial design. Nevertheless, most existing studies of multimaterial stress-constrained topology optimization consider a single isotropic yield criterion, such as von Mises [48–53], for all candidate materials, and hence, are unable to optimize fiber-reinforced composite structures governed by anisotropic yield criteria.

In this study, we propose a multimaterial stress-constrained topology optimization framework for composites incorporating dissimilar stiffness, yield strength, and yield criteria of both anisotropic (i.e., orthotropic) fiber-reinforced and isotropic candidate materials (Fig. 1). The framework simultaneously optimizes (1) geometry, (2) distribution of isotropic and anisotropic materials phases, and (3) local orientations of fiber reinforcements in anisotropic phases to design stiff, strong, and lightweight fiber-reinforced composite structures. To effectively impose local stress constraints in both anisotropic and isotropic material phases, we formulate a novel anisotropic yield function interpolation scheme to consistently integrate anisotropic (i.e., orthotropic) Tsai–Wu yield criterion for fiber-reinforced material and von Mises yield criterion for isotropic material using the load factor [37] approach, which facilitates consistent stress-violation penalization for different material types. To ensure material failure prevention at all points in the optimized structure, we use an Augmented Lagrangian (AL) based formulation to efficiently handle many local stress constraints. Using this framework, we design optimized fiber-reinforced composites with several stress-sensitive domains and various anisotropic fiber-reinforced materials with different stiffness and strength anisotropy. Further, we extend the proposed stress-constrained formulation to optimize fiber-reinforced composites simultaneously for multiple load cases. The optimized structures are verified to satisfy anisotropic Tsai–Wu and isotropic von Mises yield criteria in fiber-reinforced and isotropic candidate material phases, respectively. In addition, the introduction of isotropic materials at multi-axial joints is shown to not only increase the load-carrying efficiency of the optimized structures but also improve the stability and convergence performance of the optimization procedure. The proposed framework provides a rational design paradigm for stiff, strong, and lightweight fiber-reinforced composite structures made of both anisotropic and isotropic material phases.

The remainder of this paper is organized as follows. Section 2 introduces the design parameterization of composite structures, multimaterial stiffness interpolation scheme, and the proposed multimaterial anisotropic yield function interpolation scheme, after which the multimaterial anisotropic stress-constrained topology optimization formulation is presented. Section 3 discusses the material properties, stress constraint satisfaction (or violation) visualization schemes, and optimization parameters used in the numerical implementation of this study. Section 4 presents several design examples, including both single and multiple load cases, to demonstrate the advantages enabled by the proposed framework. Section 5 provides a few concluding remarks. Two appendices complement the paper with an elaboration on the uniform treatment of anisotropic (i.e., orthotropic) Tsai–Wu and isotropic von Mises yield criteria using load factor approach Appendix A, and a brief description of sensitivity analysis required for gradient-based optimization Appendix B.

2. Methods

This section presents a multimaterial anisotropic stress-constrained topology optimization framework used to design fiber-reinforced composite structures considering distinct stiffness, yield strength, and yield criteria of candidate anisotropic (i.e., orthotropic) fiber-reinforced and isotropic materials. We first introduce the design parameterization of fiber-reinforced composite structures and then elaborate on the multimaterial interpolation schemes for anisotropic and isotropic stiffness and yield functions, after which we present the optimization formulation and algorithm.

In the following, we present the design framework considering fiber-reinforced material with multiple pre-selected fiber orientations and isotropic material. As the anisotropic fiber-reinforced material shows distinct material properties (i.e., stiffness and strength) according to intrinsic fiber orientation, the design problem becomes similar to a multimaterial or multiphase topology optimization problem [33–35,54–60] with N_m candidate material phases, where $N_m = N_\theta + 1$ with N_θ being the number of candidate fiber orientations. Although presented for a single fiber-reinforced and a single isotropic material, the proposed framework can seamlessly incorporate multiple fiber-reinforced materials with respective pre-selected fiber orientations and multiple isotropic materials by treating them as distinct candidate material phases.

2.1. Design parameterization of fiber-reinforced composites

To parameterize fiber-reinforced composite structures, we adopt the two-field multimaterial design parameterization scheme [61,62] that simultaneously characterizes material spatial occupancy and material phase distribution. In this study, a material phase is defined as anisotropic material with a specific fiber orientation or isotropic material. In Finite Element (FE) implementation, material occupancy is characterized by design density variable $\boldsymbol{\rho}$, and material phase is determined using design material variables $\boldsymbol{\xi}^{(k)},\ k = 1, \dots, N_{\xi}$, with ρ_e and $\xi_e^{(k)}$ being the values associated with element e. The design density variable $\boldsymbol{\rho}$ determines the physical density variable $\bar{\boldsymbol{\rho}}$ that represents the solid or void in the composite with values 1 and 0, respectively. The design material variables $\boldsymbol{\xi}^{(k)},\ k = 1, \dots, N_{\xi}$, determine the physical material variables $\bar{\boldsymbol{m}}^{(i)},\ i = 1, \dots, N_m$, that represent the presence and absence of each i^{th} candidate material phase with values 1 and 0, respectively. The density and material physical variables together represent the physical multimaterial composite structure [52,63,64] (see Fig. 2). The mappings from design variables to physical variables, i.e., from $\boldsymbol{\rho}$ to $\bar{\boldsymbol{\rho}}$, and from $\boldsymbol{\xi}^{(k)},\ k = 1, \dots, N_{\xi}$, to $\bar{\boldsymbol{m}}^{(i)},\ i = 1, \dots, N_m$, are discussed as follows.

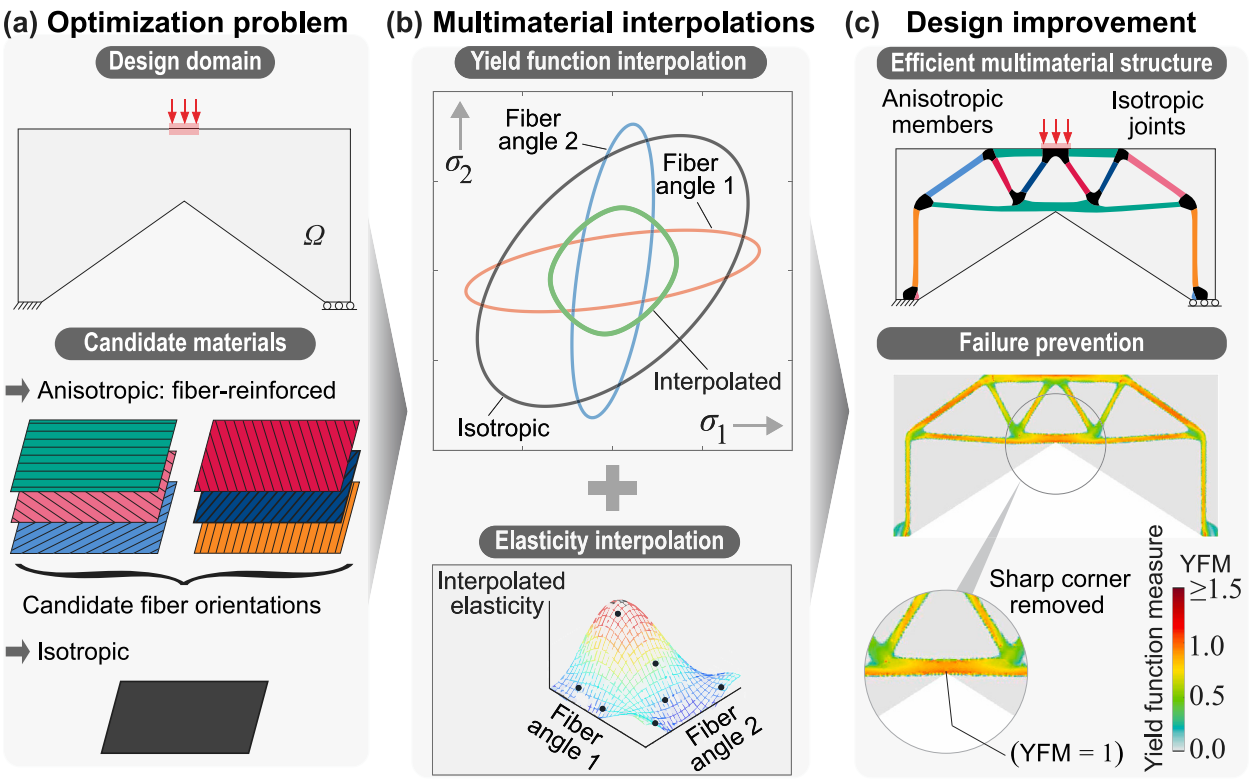

Fig. 1. Illustration of the overall goal of this study. (a) fiber-reinforced composite design problem with candidate anisotropic (i.e., orthotropic) fiber-reinforced and isotropic materials. (b) Proposed multimaterial anisotropic yield function interpolation and stiffness interpolation schemes. (c) Unique advantages of topology optimization with anisotropic stress constraints: optimized use of anisotropic and isotropic material properties, optimized geometry to prevent material yield failure by reducing local stress concentration.

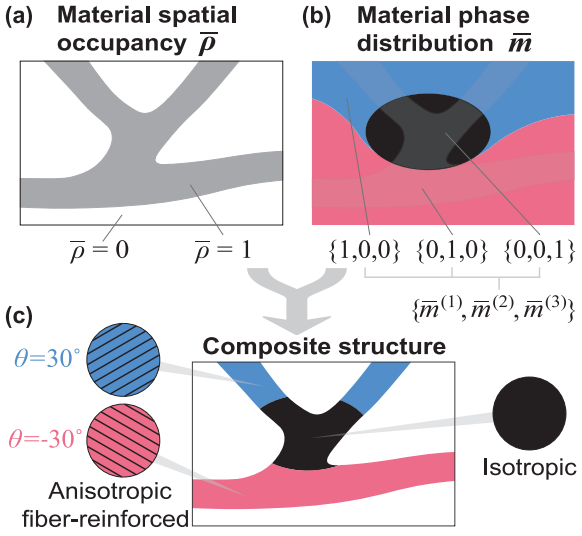

Fig. 2. Design parameterization of fiber-reinforced composites. (a) Physical density variable $\bar{\rho}$ characterizes material occupancy. (b) Physical material variables $\bar{m}^{(i)}$, $i = 1,\ldots,N_m$, determines material phase type. (c) Physical density and material variables together represent composite structures with anisotropic fiber-reinforced and isotropic materials.

2.1.1. Mapping from ρ to $\bar{\rho}$

The design density variable $\boldsymbol{\rho}$ is mapped to physical density variable $\bar{\boldsymbol{\rho}}$ through filter [65] and Heaviside projection [63], two popular schemes in topology optimization to achieve discrete and regularized, mesh-independent designs [10,65]. The physical density variable is obtained using the smoothed Heaviside projection [52,63] as

$$\tilde{\rho}_e = \frac{\tanh(\beta_\rho\gamma_\rho)+\tanh(\beta_\rho(\tilde{\rho}_e-\gamma_\rho))}{\tanh(\beta_\rho\gamma_\rho)+\tanh(\beta_\rho(1-\gamma_\rho))}, \tag{1}$$

where the projection discreteness is regulated by the Heaviside parameter β_ρ, and the projection threshold γ_ρ. The intermediate filtered variable vector [66] $\tilde{\boldsymbol{\rho}}$ is obtained by

$$\tilde{\rho}_e = \frac{\sum_{j\in \mathrm{n_e}(R_\rho)} w(\boldsymbol{x}_j)\, v_j \rho_j}{\sum_{j\in \mathrm{n_e}(R_\rho)} w(\boldsymbol{x}_j)\, v_j}, \tag{2}$$

where $\boldsymbol{x}_j$ is the centroid of element j, v_j is the corresponding element volume, R_ρ is the filter radius for density variables, $\mathrm{n_e}$ is the neighborhood of element e defined by filter radius R_ρ, i.e., $\mathrm{n_e}(R_\rho) = \left\{j : \left\|\boldsymbol{x}_j-\boldsymbol{x}_e\right\|_2 \le R_\rho\right\}$, and $w(\boldsymbol{x}_j)$ is the cubic weight function [67,68] defined as $w(\boldsymbol{x}_j) = \max\left(0, 1-\frac{\left\|\boldsymbol{x}_j-\boldsymbol{x}_e\right\|_2}{R_\rho}\right)^3$.

2.1.2. Mapping from $\xi^{(k)}$ to $\bar{m}^{(i)}$

Design material variables $\boldsymbol{\xi}^{(k)}$, $k = 1,\ldots,N_\xi$, are mapped to physical material variables $\bar{m}^{(i)}$, $i = 1,\ldots,N_m$, through two steps. First, the same filter (2) and Heaviside projection (1) operations are applied to design material variables with material variable filter radius R_ξ, Heaviside parameter β_ξ, and projection threshold γ_ξ to obtain material Heaviside projected variables $\tilde{\boldsymbol{\xi}}^{(k)}$, $k = 1,\ldots,N_\xi$. Then, material physical variables $\bar{m}^{(i)}$, $i = 1,\ldots,N_m$, are obtained from $\tilde{\boldsymbol{\xi}}^{(k)}$, $k = 1,\ldots,N_\xi$, through a tailored version of the Hypercube-to-simplex projection (HSP) scheme [13] as described below.

The HSP scheme [13] projects variables from n-dimensional hypercube to n-dimensional simplex, and satisfies the constraint $\sum_{i=1}^{n}(\bar{m}_e^{(i)}) \le 1$ implicitly. In this study, each physical material variable $\bar{m}_e^{(i)}$ represents the portion of i^{th} candidate material phase in an element e, and they need to satisfy the condition $\sum_{i=1}^{N_m}(\bar{m}_e^{(i)}) = 1$ for a physical structure.

To satisfy the equality condition, we use HSP to obtain the first (N_m-1) physical material variables and make the last physical material variable dependent. With this tailored HSP scheme, we use $N_\xi = (N_m - 1)$ material Heaviside projected variables to obtain N_m physical material variables as

$$\begin{aligned} &\bar{m}_e^{(i)} = \sum_{j=1}^{2^{(N_m-1)}} b_j^{(i)} \left((-1)^{(N_m-1+\sum_{k=1}^{N_m-1} c_j^{(k)})} \prod_{k=1}^{(N_m-1)} (\bar{\xi}_e^{(k)} + c_j^{(k)} - 1) \right), \\ &\qquad i = 1, \dots, N_m - 1, \\ &\text{and,} \quad \bar{m}_e^{(N_m)} = 1 - \sum_{i=1}^{N_m-1} (\bar{m}_e^{(i)}) \end{aligned} \tag{3}$$

where, $c_j^{(i)} = \{0, 1\}$ is the j^{th} vertex of $(N_m - 1)$-dimensional unit hypercube for the i^{th} candidate material, and $b_j^{(i)}$ is the mapped vertex of $(N_m - 1)$-dimensional standard simplex domain calculated as

$$b_j^{(i)} = \begin{cases} \dfrac{c_j^{(i)}}{\sum_{i=1}^{N_m-1} c_j^{(i)}}, & \text{if } \sum_{i=1}^{N_m-1} c_j^{(i)} \geq 1 \\ 0, & \text{otherwise.} \end{cases} \tag{4}$$

2.2. Stiffness interpolation scheme

This subsection discusses the multimaterial stiffness interpolation scheme for the mechanical behavior characterization of fiber-reinforced composites. For N_m candidate material phases, the general interpolated stiffness tensor $\mathbf{C}_e^{(\xi)}$ for an element e is obtained by the Solid Isotropic Material with Penalization (SIMP) [61,69] through $\bar{\rho}_e$ combined with a SIMP-like interpolation through $\bar{m}_e^{(i)}$, $i = 1, \dots, N_m$, [19,52,55,62,64], i.e.,

$$\mathbf{C}_e^{(\xi)}(\bar{\rho}_e, \bar{m}_e^{(1)}, \dots, \bar{m}_e^{(N_m)}) = \left[\varepsilon + (1-\varepsilon)\bar{\rho}_e^{p_\rho}\right] \sum_{i=1}^{N_m} (\bar{m}_e^{(i)})^{p_\xi} \mathbf{C}^{(i)}, \tag{5}$$

where $\mathbf{C}^{(i)}$ is the stiffness tensor of the i^{th} candidate material phase, p_ρ and p_ξ are the penalization parameters associated with density and material variables, respectively, and ε is a small number to avoid the numerical singularity. The interpolated stiffness tensor $\mathbf{C}_e^{(\xi)}$ becomes identical to $\mathbf{C}^{(i)}$ when $\bar{\rho}_e = 1$ and $\bar{m}_e^{(i)} = 1$. We note that $\mathbf{C}_e^{(\xi)}$ is physically well-defined only when $\bar{\rho}_e, \bar{m}_e^{(1)}, \dots, \bar{m}_e^{(N_m)} \in \{0, 1\}$, which is enforced by the Heaviside projection technique [52,63] at the later stage of the optimization. Therefore, interpolation (5) represents a numerical scheme commonly used to facilitate design optimization rather than computing the homogenized properties.

In this study, the set of N_m candidate material phases in interpolation (5) includes N_θ different fiber orientations of the anisotropic fiber-reinforced material that require stiffness tensor transformations from respective fiber (local) coordinates to design-domain (global) coordinates. The transformed anisotropic (i.e., orthotropic) stiffness tensor $\mathbf{C}^{(i)}$ in global coordinates is obtained as

$$\mathbf{C}^{(i)} = \mathbf{T}^{-1}(\theta^{(i)}) \mathbf{C}^{(\text{aniso})} \mathbf{T}^{-T}(\theta^{(i)}), \qquad i = 1, \dots, N_\theta, \tag{6}$$

where $\theta^{(i)}$ is the i^{th} fiber orientation with respect to the global coordinates, $\mathbf{C}^{(\text{aniso})}$ is the anisotropic (i.e., orthotropic) stiffness tensor in the fiber coordinates, and $\mathbf{T}(\theta)$ is the transformation tensor corresponding to a fiber orientation θ. Using interpolation (5) and anisotropic stiffness tensor transformation (6), we derive the stiffness interpolation scheme for composite structure with anisotropic (i.e., orthotropic) fiber-reinforced and isotropic materials as

$$\begin{aligned} &\mathbf{C}_e^{(\xi)}(\bar{\rho}_e, \bar{m}_e^{(1)}, \dots, \bar{m}_e^{(N_m)}) = \\ &\quad \left[\varepsilon + (1-\varepsilon)\bar{\rho}_e^{p_\rho}\right] \left(\sum_{i=1}^{N_\theta} (\bar{m}_e^{(i)})^{p_\xi} \left(\mathbf{T}^{-1}(\theta^{(i)}) \mathbf{C}^{(\text{aniso})} \mathbf{T}^{-T}(\theta^{(i)}) \right) \right. \\ &\quad \left. + (\bar{m}_e^{(N_\theta+1)})^{p_\xi} \mathbf{C}^{(\text{iso})} \right), \end{aligned} \tag{7}$$

where $\mathbf{C}^{(\text{iso})}$ is the stiffness tensor of the candidate isotropic material.

For 2D plane stress problems used in this study, the matrix forms of the stiffness tensors $\mathbf{C}^{(\text{aniso})}$ and $\mathbf{C}^{(\text{iso})}$ are given by

$$\begin{aligned} \mathbf{C}^{(\text{aniso})} &= \begin{bmatrix} \frac{E_{11}}{1-\nu_{12}\nu_{21}} & \frac{\nu_{12}E_{22}}{1-\nu_{12}\nu_{21}} & 0 \\ \frac{\nu_{12}E_{22}}{1-\nu_{12}\nu_{21}} & \frac{E_{22}}{1-\nu_{12}\nu_{21}} & 0 \\ 0 & 0 & G_{12} \end{bmatrix}, \quad \text{and,} \\ \mathbf{C}^{(\text{iso})} &= \frac{E_{\text{iso}}}{1-\nu_{\text{iso}}^2} \begin{bmatrix} 1 & \nu_{\text{iso}} & 0 \\ \nu_{\text{iso}} & 1 & 0 \\ 0 & 0 & \frac{1-\nu_{\text{iso}}}{2} \end{bmatrix}, \end{aligned} \tag{8}$$

and the matrix form of the transformation tensor $\mathbf{T}(\theta)$ is given by

$$\mathbf{T}(\theta) = \begin{bmatrix} \cos^2(\theta) & \sin^2(\theta) & 2\sin(\theta)\cos(\theta) \\ \sin^2(\theta) & \cos^2(\theta) & -2\sin(\theta)\cos(\theta) \\ -\sin(\theta)\cos(\theta) & \sin(\theta)\cos(\theta) & \cos^2(\theta) - \sin^2(\theta) \end{bmatrix}, \tag{9}$$

where E_{11}, E_{22}, ν_{12}, and G_{12} are elastic modulus along the fiber direction, elastic modulus perpendicular to the fiber direction, Poisson's ratio with respect to the fiber direction, and shear modulus, respectively, for the anisotropic (i.e., orthotropic) fiber-reinforced material, and E_{iso} and ν_{iso} are elastic modulus and Poisson's ratio, respectively, for the isotropic material.

2.3. Anisotropic yield function interpolation scheme

This subsection presents the proposed anisotropic yield function interpolation scheme that simultaneously incorporates both anisotropic (i.e., orthotropic) and isotropic materials in stress-constrained topology optimization. For N_m candidate material phases, the general interpolated yield function $f_e^{(\xi)}$ is obtained by a SIMP-like interpolation of yield functions through physical material variables $\bar{m}_e^{(i)}$, $i = 1, \dots, N_m$, [70], i.e.,

$$f_e^{(\xi)}(\bar{m}_e^{(1)}, \dots, \bar{m}_e^{(N_m)}, \boldsymbol{\sigma}_e^{(1)}, \dots, \boldsymbol{\sigma}_e^{(N_m)}) = \sum_{i=1}^{N_m} (\bar{m}_e^{(i)})^{p_{f_\xi}} f^{(i)}(\boldsymbol{\sigma}_e^{(i)}), \tag{10}$$

where $\boldsymbol{\sigma}_e^{(i)} := \mathbf{C}^{(i)}\boldsymbol{\epsilon}_e$ is the stress state corresponding to i^{th} candidate material phase for element e computed from element strain $\boldsymbol{\epsilon}_e$, and p_{f_ξ} is a penalization parameter. The yield function $f^{(i)}(\boldsymbol{\sigma})$ associated with i^{th} candidate material phase is given as

$$f^{(i)}(\boldsymbol{\sigma}^{(i)}) \leq 1, \quad i = 1, \dots, N_m, \tag{11}$$

where the equality condition represents the corresponding yield surfaces. This study considers von Mises yield criterion [71] for the isotropic material, which is expressed as

$$f^{(\text{vm})}(\boldsymbol{\sigma}) = \frac{\sigma_{\text{vm}}(\boldsymbol{\sigma})}{\bar{\sigma}_{\text{iso}}} \leq 1, \tag{12}$$

where $\sigma_{\text{vm}}(\boldsymbol{\sigma}) = \sqrt{\sigma_{xx}^2 + \sigma_{yy}^2 - \sigma_{xx}\sigma_{yy} + 3\sigma_{xy}^2}$ is the plane-stress von Mises stress, with σ_{xx}, σ_{yy}, and σ_{xy} being in-plane stress components in global coordinates, and $\bar{\sigma}_{\text{iso}}$ is the strength of the isotropic material. For the anisotropic (i.e., orthotropic) material, this study adopts the Tsai–Wu yield criterion [72] to represent fiber-reinforced material failure, which is expressed (for a 2D plane stress problem) as

$$f^{(\text{tw})}(\boldsymbol{\sigma}, \theta) = F_{11}\sigma_{11}^2 + F_{22}\sigma_{22}^2 + F_{66}\sigma_{12}^2 + F_{12}\sigma_{11}\sigma_{22} + F_1\sigma_{11} + F_2\sigma_{22} \leq 1. \tag{13}$$

where σ_{11}, σ_{22}, and σ_{12} are the in-plane stress components with respect to the fiber orientation (i.e., in local fiber coordinates) obtained by transforming the global coordinates in-plane stress components as

$$\begin{bmatrix} \sigma_{11} \\ \sigma_{22} \\ \sigma_{12} \end{bmatrix} = \mathbf{T}(\theta) \begin{bmatrix} \sigma_{xx} \\ \sigma_{yy} \\ \sigma_{xy} \end{bmatrix}, \tag{14}$$

where $\mathbf{T}(\theta)$ is the transformation matrix (9). Given the Tsai–Wu material strength parameters X_t, X_c, Y_t, Y_c, and S for a plane stress

orthotropic material, the coefficients in the Tsai–Wu yield criterion (13) are obtained as

$$\begin{aligned} &F_1 = \frac{1}{X_t} - \frac{1}{X_c}, F_2 = \frac{1}{Y_t} - \frac{1}{Y_c}, \\ &F_{11} = \frac{1}{X_t \cdot X_c}, F_{22} = \frac{1}{Y_t \cdot Y_c}, F_{66} = \frac{1}{S \cdot S}, \\ &F_{12} = -0.5\sqrt{F_{11}F_{22}}, \end{aligned} \tag{15}$$

where X denotes the strength along the fiber orientation, Y denotes the strength perpendicular to the fiber orientation, S denotes the shear strength, and subscripts c and t represent cases for compression and tension, respectively.

Directly using the actual form of Tsai–Wu yield criterion (13) together with the von Mises yield criterion (12) in the interpolation (10) leads to inconsistent stress-violation penalization (see Appendix A). To address this problem of inconsistent penalization, we present an equivalent Tsai–Wu yield criterion based on the concept of load factor [37] as

$$\eta^{(\mathrm{tw})}(\boldsymbol{\sigma}, \theta) = \frac{2A(\boldsymbol{\sigma}, \theta)}{\sqrt{B^2(\boldsymbol{\sigma}, \theta) + 4A(\boldsymbol{\sigma}, \theta)} - B(\boldsymbol{\sigma}, \theta)} \leq 1, \tag{16}$$

where, $A(\boldsymbol{\sigma}, \theta) = F_{11}\sigma_{11}^2 + F_{22}\sigma_{22}^2 + F_{66}\sigma_{12}^2 + F_{12}\sigma_{11}\sigma_{22}$, and $B(\boldsymbol{\sigma}, \theta) = F_1\sigma_{11} + F_2\sigma_{22}$. To avoid division by zero, the minimum value of $A(\boldsymbol{\sigma}, \theta)$ is set to 1×10^{-12}. Notice that, for a special case with $X_t = X_c = Y_t = Y_c = \sqrt{3}S = \bar{\sigma}_{\mathrm{iso}}$, the load factor-based Tsai–Wu criterion (16) and von Mises criterion (12) become identical. This property of load factor facilitates consistent penalization from both anisotropic (i.e., orthotropic) Tsai–Wu and the isotropic von Mises yield criteria for the same extent of stress violation. Moreover, the load factor represents a proportional measure of stress violation with respect to the origin in the principal stress plane, enabling uniform penalization for tension and compression stress violation in the case of anisotropic Tsai–Wu strength. A detailed discussion of the justification for using this load factor-based Tsai–Wu yield criterion is provided in Appendix A.

Using the interpolation (10) and load factor-based Tsai–Wu criterion (16), we propose the interpolated yield function $f_e^{(\xi)}(\cdot)$ for composite structures with anisotropic (i.e., orthotropic) Tsai–Wu and isotropic von Mises candidate materials as,

$$\begin{aligned} f_e^{(\xi)}\left(\bar{m}_e^{(1)}, \ldots, \bar{m}_e^{(N_m)}, \boldsymbol{\sigma}^{(1)}, \ldots, \boldsymbol{\sigma}^{(N_m)}\right) &= \textstyle\sum_{i=1}^{N_\theta} (\bar{m}_e^{(i)})^{p_{f_\xi}} \eta^{(\mathrm{tw})}\left(\boldsymbol{\sigma}^{(i)}, \theta^{(i)}\right) \\ &+ (\bar{m}_e^{(N_\theta+1)})^{p_{f_\xi}} f^{(\mathrm{vm})}\left(\boldsymbol{\sigma}^{(\mathrm{iso})}\right) \leq 1, \end{aligned} \tag{17}$$

where $\boldsymbol{\sigma}^{(i)}$ is the stress state of i^{th} fiber orientation of the anisotropic material in the global coordinates, and $\boldsymbol{\sigma}^{(\mathrm{iso})}$ is the stress state of the isotropic material. Fig. 3 illustrates the yield function interpolation (17) with three candidate material phases consisting of two candidate fiber orientations of an anisotropic material and a candidate isotropic material. The interpolated yield surface undergoes a gradual transition from the actual yield surface of one material to another according to the change in physical material variable values.

We remark that the proposed anisotropic yield function interpolation scheme (17) incorporates the material strength information, i.e., distinct yield strength and criteria of both anisotropic (i.e., orthotropic) and isotropic candidate materials in the design framework. The material strength information is realized as appropriate anisotropic and isotropic stress constraints in the optimization formulation presented below. The goal is to ensure that the optimized design performs entirely in the elastic deformation range, i.e., without any local material failure or plasticity under the prescribed loading.

2.4. Optimization formulation

Based on the proposed multimaterial anisotropic yield function interpolation scheme (17), we formulate the topology optimization problem as weighted compliance-volume minimization with stress constraints and multiple load cases to design stiff and lightweight fiber-reinforced composite structures while preventing local material failure. Here, we assume all candidate material phases have the same mass densities, and thus reducing total structural volume is equivalent to reducing total structural weight. We use the polynomial stress constraint [67,68] to increase the penalty for severe constraint violation and accelerate optimization convergence. The topology optimization formulation is stated as

$$\begin{aligned} \min_{\boldsymbol{\rho}, \boldsymbol{\xi}^{(1)}, \ldots, \boldsymbol{\xi}^{(N_\xi)}} \quad & J\left(\boldsymbol{\rho}, \boldsymbol{\xi}^{(1)}, \ldots, \boldsymbol{\xi}^{(N_\xi)}\right) = \frac{w}{N_l} \sum_{l=1}^{N_l} C_l + (1-w)V \\ \text{s.t.} \quad & g_{e,l}\left(\boldsymbol{\rho}, \boldsymbol{\xi}^{(1)}, \ldots, \boldsymbol{\xi}^{(N_\xi)}, \mathbf{U}_l\right) = \left[\varepsilon + (1-\varepsilon)\bar{\rho}_e(\boldsymbol{\rho})^{p_\rho}\right]\left(\Lambda_{e,l}^3 \right. \\ & \left. + \Lambda_{e,l}\right) \leq 0, \\ & \qquad\qquad e = 1, \ldots, N_e, \quad l = 1, \ldots, N_l, \\ & \rho_e \in [0,1], \qquad e = 1, \ldots, N_e, \\ & \xi_e^{(k)} \in [0,1], \qquad e = 1, \ldots, N_e, \quad k = 1, \ldots, N_\xi, \\ \text{with:} \quad & \mathbf{K}\left(\boldsymbol{\rho}, \boldsymbol{\xi}^{(1)}, \ldots, \boldsymbol{\xi}^{(N_\xi)}\right)\mathbf{U}_l = \mathbf{F}_l^{\mathrm{ext}}, \qquad l = 1, \ldots, N_l, \end{aligned} \tag{18}$$

where $C_l = (\mathbf{F}_l^{\mathrm{ext}})^T\mathbf{U}(\boldsymbol{\rho}, \boldsymbol{\xi}^{(1)}, \ldots, \boldsymbol{\xi}^{(N_\xi)})/C_l^*$ is the normalized end-compliance corresponding to load case l with C_l^* being the end-compliance of uniform initial guess, $V = \left(\sum_{e=1}^{N_e} \bar{\rho}_e(\boldsymbol{\rho})v_e\right) / \sum_{e=1}^{N_e} v_e$ is the total structural volume fraction with v_e being the volume of element e, $w \in [0,1]$ is a weight factor for the compliance terms in the objective, $\Lambda_{e,l} = \left(f_{e,l}^{(\xi)}(\boldsymbol{\xi}^{(1)}, \ldots, \boldsymbol{\xi}^{(N_\xi)}, \mathbf{U}_l(\boldsymbol{\rho}, \boldsymbol{\xi}^{(1)}, \ldots, \boldsymbol{\xi}^{(N_\xi)})) - 1\right)$ is obtained from the interpolated yield function value (17) associated with element e corresponding to load case l, $\mathbf{K}\left(\boldsymbol{\rho}, \boldsymbol{\xi}^{(1)}, \ldots, \boldsymbol{\xi}^{(N_\xi)}\right)$ is the global stiffness matrix obtained from the interpolated stiffness (7), $\mathbf{U}_l$ and $\mathbf{F}_l^{\mathrm{ext}}$ are the global displacement vector and the global external force vector corresponding to load case l, respectively, N_e is the total number of elements in the FE mesh, and N_l is the number of load cases. For the uniform initial guess, the initial values of design density variables are set to $\rho_e = 0.5$, and the initial values of the design material variables are set to $\xi_e^{(1)} = \cdots = \xi_e^{(N_\xi)} = 0.25$, so that all physical material variables, $\bar{m}_e^{(1)}, \ldots, \bar{m}_e^{(N_m)}$, have equal values after the HSP projection. Notably, volume fractions of different materials are not restricted in the formulation, and their appearance in the final design is determined solely by the optimizer to facilitate the optimized use of different anisotropic and isotropic material properties.

Solving the optimization problem (18) is highly challenging due to the $N_l \times N_e$ nonlinear local stress constraints. Most multimaterial stress-constrained topology optimization studies use approximate aggregation methods, such as the p-norm approach [73], to cluster the $N_l \times N_e$ constraints into a single or a handful of constraints. However, using such global aggregation approach to constrain an intrinsically local quantity like stress may cause numerical issues in the optimized designs [68]. To solve the optimization problem (18) while preserving the local nature of stress constraints, this study adopts the Augmented Lagrangian (AL) method [74,75], which is successfully employed in the literature to solve single-material stress-constrained topology optimization problems [67,68,76–82].

The AL method transforms the original constrained optimization problem into a series of (augmented) unconstrained optimization sub-problems. The local stress constraints are augmented to the original objective function using Lagrangian parameter estimators associated with each local constraint and a penalty term. The unconstrained optimization sub-problems are solved sequentially, i.e., the Lagrangian parameter estimators and the penalty term are updated after solving the current sub-problem and then used to solve the next sub-problem. Specifically, the unconstrained optimization sub-problem at the n^{th} optimization step is given by [80]

$$\begin{aligned} \min_{\boldsymbol{\rho}', \boldsymbol{\xi}'^{(1)}, \ldots, \boldsymbol{\xi}'^{(N_\xi)}} \psi^{(n)}\left(\boldsymbol{\rho}', \boldsymbol{\xi}'^{(1)}, \ldots, \boldsymbol{\xi}'^{(N_\xi)}\right) &= J\left(\boldsymbol{\rho}', \boldsymbol{\xi}'^{(1)}, \ldots, \boldsymbol{\xi}'^{(N_\xi)}\right) + \\ \sum_{l=1}^{N_l}\left[\frac{1}{N_e}\sum_{e=1}^{N_e}\left(\lambda_{e,l}^{(n)} h_{e,l}^{(n)}\left(\boldsymbol{\rho}', \boldsymbol{\xi}'^{(1)}, \ldots, \boldsymbol{\xi}'^{(N_\xi)}\right)\right.\right. & \\ \left.\left. + \frac{\mu^{(n)}}{2} h_{e,l}^{(n)}\left(\boldsymbol{\rho}', \boldsymbol{\xi}'^{(1)}, \ldots, \boldsymbol{\xi}'^{(N_\xi)}\right)^2\right)\right], & \end{aligned} \tag{19}$$

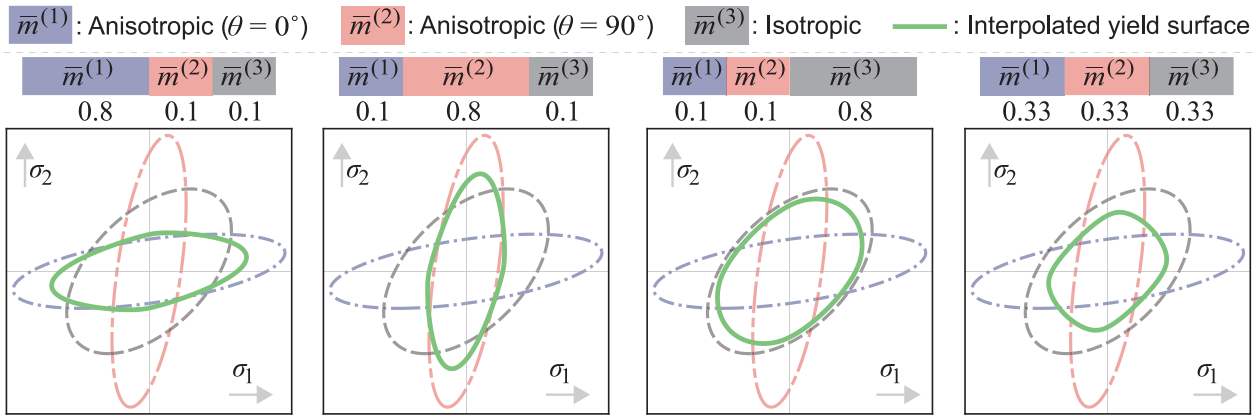

Fig. 3. Transformation of interpolated yield function for different $\bar{m}^{(1)}, \bar{m}^{(2)}, \bar{m}^{(3)}$ values considering three candidate material phases that include two fiber orientations of the anisotropic material and the isotropic material.

where $\psi^{(n)}\left(\rho', \xi'^{(1)}, \ldots, \xi'^{(N_\xi)}\right)$ is the n^{th} step (augmented) objective function with ρ' and $\xi'^{(1)}, \ldots, \xi'^{(N_\xi)}$ denoting dummy design variables corresponding to ρ and $\xi^{(1)}, \ldots, \xi^{(N_\xi)}$, and $h_{e,l}\left(\rho', \xi'^{(1)}, \ldots, \xi'^{(N_\xi)}\right)$ is the equality constraint for e^{th} element and load case l given by

$$h_{e,l}^{(n)}\left(\rho', \xi'^{(1)}, \ldots, \xi'^{(N_\xi)}\right) = \max\left(g_{e,l}\left(\rho', \xi'^{(1)}, \ldots, \xi'^{(N_\xi)}, \mathbf{U}_l(\rho', \xi'^{(1)}, \ldots, \xi'^{(N_\xi)})\right), -\frac{\lambda_{e,l}^{(n)}}{\mu^{(n)}}\right), \tag{20}$$

where $\lambda_{e,l}^{(n)}$ is an estimate of the Lagrange multiplier estimator for e^{th} element and load case l, and $\mu^{(n)}$ is a penalty coefficient. The updated design variables for the next sub-problem are the solution of the current sub-problem (19), i.e., $\rho^{(n+1)} = \rho'^{*}$ and $\{\xi'^{(1)}, \ldots, \xi'^{(N_\xi)}\}^{(n+1)} = \{\xi'^{(1)}, \ldots, \xi'^{(N_\xi)}\}^{*}$. The Lagrange multiplier estimators and the penalty coefficient for the next sub-problem are obtained from the updated design variables as

$$\mu^{(n+1)} = \max\left(\alpha\mu^{(n)}, \mu^{(\max)}\right) \text{ and}$$
$$\lambda_{e,l}^{(n+1)} = \lambda_{e,l}^{(n)} + \mu^{(n)} h_{e,l}^{(n)}\left(\rho^{(n+1)}, \{\xi'^{(1)}, \ldots, \xi'^{(N_\xi)}\}^{(n+1)}\right), \tag{21}$$

where $\alpha > 1$ is a constant, and $\mu^{(\max)}$ is an upper bound for the penalty coefficient to avoid numerical instability. This study uses the gradient-based optimizer Method of Moving Asymptotes (MMA) [83] to solve the unconstrained sub-problems. The gradient expressions with respect to the design variables are provided in Appendix B.

We note that composite laminate structures (one example of fiber-reinforced structures) usually include different ply arrangements for several advantages. However, the capability of topology optimization to design composites for improved stiffness and strength simultaneously considering both anisotropic and isotropic material phases has not been established, even for uniaxial fiber-reinforced materials and one-ply laminates. Thus, the main objective and contribution of this work are to propose optimization formulation and solution schemes to enable this capability.

In the presented design examples, the anisotropic candidate material phases consist of uniaxial fiber orientations to provide maximum stiffness and strength per unit volume to the structure, assuming a given fiber–matrix ratio. However, laminate candidate material phases with different ply arrangements may be included in the optimization for different objective and constraint functions, which benefit from having fibers in multiple directions throughout the cross-section.

In terms of applications, the proposed methodology is not restricted to laminates and can be readily applied to other anisotropic composite structures that have uniaxially oriented fibers throughout or parts of their cross-sections, as long as the stiffness tensor and yield function representing stiffness and strength of the entire cross-section can be characterized. Furthermore, the presented framework can also be extended to include laminates containing multiple plies arrangements, which may be preferable in practice as candidate material phases, if their overall stiffness tensors and yield/failure surfaces can be characterized. For example, the isotropic candidate material may be replaced by a laminate phase with multiple ply directions throughout its cross-section, with a characterized stiffness tensor and yield/failure surface.

3. Numerical implementation

This section describes the numerical implementation of the proposed framework. The optimization formulation, including finite element analysis and iterative optimization updates using MMA, is implemented using a Matlab code developed in-house. In the following, we briefly discuss the candidate material properties, visualization schemes to verify material yield criteria satisfaction or violation, and optimization parameter values used for the fiber-reinforced composite design examples in Section 4.

3.1. Material properties used in the numerical examples

This study uses four different fiber-reinforced materials throughout the design examples presented in Section 4, namely TM800s/M21, Kevlar/epoxy, Graphite/epoxy, and laminated bamboo lumber (LBL). We remark that the proposed formulation can also be applied to account for other anisotropic (i.e., orthotropic) materials laminates. Thus, we also consider LBL as a demonstration. Among these materials, TM800s/M21 has the Tsai–Hill yield criterion, which is a special case of the Tsai–Wu criterion when $X_t = X_c$, and $Y_t = Y_c$. The other three fiber-reinforced materials have the Tsai–Wu yield criteria with different strength parameters. Each design case from the numerical examples uses any one of these four anisotropic fiber-reinforced materials and a suitable isotropic material with the von Mises yield criterion. The material properties, i.e., stiffness and strength parameters of the fiber-reinforced materials and corresponding isotropic materials, adopted in the design examples are listed in Table 1.

This study assumes the yield strength parameters are obtained corresponding to the stress states till which the material behavior is linear elastic. For brittle materials such as Graphite/epoxy, we use strength parameters corresponding to their failure criteria. For ductile materials, we assume strength parameters (e.g., von Mises strength) corresponding to material yielding due to the onset of plasticity.

Table 1
Material properties of candidate anisotropic (i.e., orthotropic) fiber-reinforced and corresponding isotropic materials (units: MPa).

Fiber-reinforced material	Anisotropic stiffness parameters				Anisotropic Tsai–Wu strength parameters					Corresponding isotropic material properties		
	E_{11}	E_{22}	ν_{12}	G_{12}	X_t	X_c	Y_t	Y_c	S	E_{iso}	ν_{iso}	$\bar{\sigma}_{iso}$
TM800s/M21	135×10^3	7.64×10^3	0.35	5.61×10^3	165	165	45	45	50	85.6×10^3	0.3	165
Kevlar/epoxy	100×10^3	6.9×10^3	0.33	2.1×10^3	1380	280	35	105	40	64×10^3	0.3	280
Graphite/epoxy	181×10^3	10.3×10^3	0.28	7.17×10^3	1500	1500	40	246	68	114.8×10^3	0.3	1500
LBL	9913.5	1853.9	0.31	1164.8	90	77	2	22	16	7060.4	0.3	55

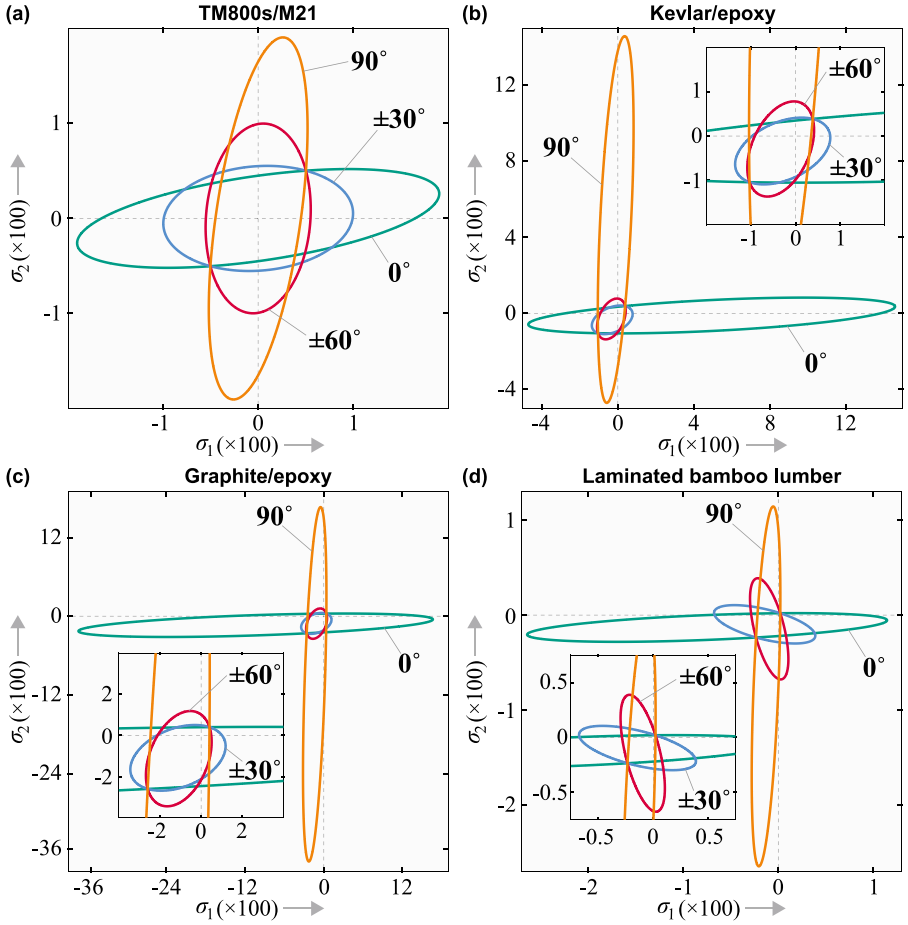

Fig. 4. Tsai–Wu yield surface transformations with different fiber orientations θ_p with respect to principal stress σ_1 for different fiber-reinforced materials: (a) TM800s/M21, (b) Kevlar/epoxy, (c) Graphite/epoxy, (d) Laminated bamboo lumber (LBL).

3.2. Stress-constraint satisfaction visualization schemes

This study adopts two approaches, *(1)* yield function measure (YFM), and *(2)* principal stress plot with appropriate yield surface, to visualize and verify the satisfaction or violation of anisotropic and isotropic stress constraints. These approaches are extended from the two common practices in stress-constrained topology optimization studies, including normalized von Mises stress plot [68], and principal stress plot together with von Mises yield surface [68], for the optimized structure.

In the first approach, the yield function measure is defined as $\text{YFM} = [\epsilon + (1-\epsilon)\tilde{\rho}_e^{p_\rho}]f_e^{(\xi)}$, with $f_e^{(\xi)}$ being the interpolated yield function (17). For a solid element with a single material phase, the YFM value becomes the same as the yield function value for that occupying material for a certain stress state. Naturally, this YFM is equivalent to von Mises stress normalized with the von Mises strength in the case of isotropic material. The second approach uses principal stresses together with actual yield surface for the isotropic material, and a yield surface contour for the anisotropic material, which is described as follows.

First, we illustrate the anisotropic Tsai–Wu yield function transformations with different fiber orientations for each fiber-reinforced material from Table 1. We plot the transformed Tsai–Wu yield surfaces corresponding to $\theta_p = 0°, \pm30°, \pm45°, \pm60°$, and 90° in principal stress $\sigma_1 - \sigma_2$ plane (see Fig. 4), where θ_p is the angle between the fiber direction and the direction of principal stress σ_1, assuming $\sigma_1 \geq \sigma_2$. Physically, this transformation of the Tsai–Wu yield function with fiber orientation signifies the gradual reduction in effective material strength as the fiber orientation is rotated from the principal stress or load path direction. In an optimized design, different elements may have different principal stress directions, leading to a wide range of θ_p for a limited pre-selected fiber orientation θ defined with respect to the global axes. Therefore, we construct a Tsai–Wu yield surface contour by taking the union of the transformed Tsai–Wu yield surfaces for all possible orientations ($\theta_p \in [-90°, 90°]$), and plot it together with the principal stresses of all solid anisotropic elements in the optimized design. Principal stress points for all candidate fiber orientations of the anisotropic material staying inside the Tsai–Wu yield surface contour denote a necessary but not sufficient condition for anisotropic stress-constraint satisfaction. Fig. 5 shows the Tsai–Wu yield surface contour

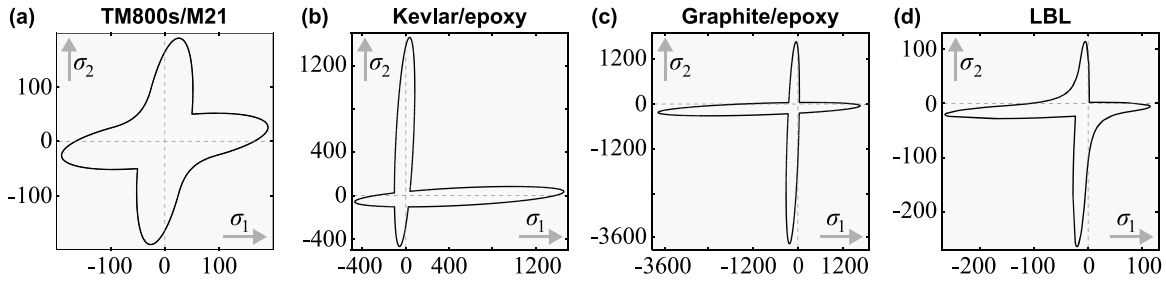

Fig. 5. Tsai–Wu yield surface contours obtained from the transformed yield surfaces of 180 equally-spaced fiber orientations ($\theta_p \in [-90°, 90°]$) for different fiber-reinforced materials: (a) TM800s/M21, (b) Kevlar/epoxy, (c) Graphite/epoxy, (d) Laminated bamboo lumber (LBL).

Table 2
AL parameters used in all the examples.

Parameter	Value
Initial Lagrange multiplier estimators, $\lambda_e^{(0)}$	0
Initial penalty coefficient, $\mu^{(0)}$	10
Maximum penalty coefficient, $\mu_{\max}$	10000
Penalty update factor, α	1.05
Number of MMA iterations per AL step	5
Maximum number of AL steps	1300
Convergence tolerance on density design variables	0.0015
Convergence tolerance on stress constraints	0.003

estimated by taking the union of Tsai–Wu yield surfaces corresponding to 180 equally-spaced fiber orientations between −90° and 90° for each fiber-reinforced material from Table 1.

3.3. Optimization parameters used in the numerical examples

Regarding topology optimization of the numerical examples, we use the following setup for penalization parameters and Heaviside projections. For all design cases, p_ρ is assigned 3 from the start, and p_ξ increases from 1 to 3 with an increment of 0.5 at every 50 steps, starting from step 80. The penalty parameter p_{f_ξ} is also increased together with p_ξ from 1 to 3. After p_ξ and p_{f_ξ} reach the value 3, the Heaviside projections for both density and material variable start with $\beta_\rho = \beta_\xi = 1$, which are doubled every 30 steps till they reach respective maximum values $\beta_\rho^{(\max)} = 30$, and $\beta_\xi^{(\max)} = 128$. The Heaviside threshold parameters for both density and material variables are taken as $\gamma_\rho = \gamma_\xi = 0.5$ throughout the optimization. After both the Heaviside projection is completed, the p_{f_ξ} decreases from 3 to 1 with a decrement of 0.2 at every 80 steps. Finally, the optimization is terminated when a prescribed maximum number of AL steps is reached or a prescribed tolerance for the stress constraints is achieved after the p_{f_ξ} is decreased to 1. The values of the AL parameters and convergence tolerances for all numerical examples are provided in Table 2.

Generally, the weight factor w controls the trade-off of compliance and volume of the optimized design. A smaller w will lead to optimized structures with smaller volumes and larger compliance, while a larger w will lead to structures with larger volumes and smaller compliance. In this study, two values are considered for the compliance weight factor w in the numerical examples. We use $w = 0.25$ for Examples 1 and 2, and set $w = 0.3$ for Example 3. Suitable weight factor values may vary depending on the candidate material properties, design domain, number of available candidate material phases, and desired stiffness and strength performance from the optimized structure. It will be valuable to investigate the influence of the weight factor and suitable optimization parameter update scheme on the optimized design, which is an interesting direction for future study.

4. Results and discussions

This section presents three numerical examples of optimized fiber-reinforced composite designs obtained using the proposed framework. The first example shows the effective prevention of local failure empowered by the anisotropic stress constraints. It also demonstrates the unique advantage of using isotropic material in the multi-axial load paths at fiber composite joints. The second example investigates the influence of various Tsai–Wu strength anisotropy on the optimized designs using different fiber-reinforced materials. Both the first and second examples consider $N_l = 1$, i.e., single load cases. The third example applies the proposed formulation to a multiple load case problem and demonstrates simultaneous stress constraint satisfaction for all load cases. A summary of the highlights and features of these examples is given in Table 3.

4.1. Example 1: Merits of anisotropic stress constraints and isotropic material in fiber-reinforced composites

The first example compares the proposed framework with two different fiber-reinforced composite topology optimization approaches to demonstrate the unique advantages of *(1)* anisotropic stress constraints in local failure prevention with suitable topology, and *(2)* isotropic materials in strengthening multi-axially loaded joints in fiber-reinforced composite design optimization. Fig. 6(a) shows the portal design domain with prescribed boundary conditions (BCs), the candidate fiber orientations of the anisotropic fiber-reinforced material TM800s/M21 and the corresponding candidate isotropic material with elastic and strength properties from Table 1, and the features of three design cases to be compared. Among the three design cases, Dsg. 1 is optimized using only TM800s/M21 without stress constraints, Dsg. 2 is optimized using only TM800s/M21 while considering corresponding anisotropic Tsai–Hill stress constraints, and Dsg. 3 is optimized using both the anisotropic TM800s/M21 and corresponding isotropic candidate material while considering respective Tsai–Hill and von Mises stress constraints. We use compliance weight factor $w = 0.25$ for all three design cases.

Fig. 6(b) compares Dsg. 1 and Dsg. 3 to demonstrate the significance of anisotropic stress constraints in the fiber-reinforced composite design optimization. Without any stress constraints, the optimized design of Dsg. 1 shows a sharp corner with high localized stress, where the corresponding YFM fringe plot reveals material failure with a YFM value of 5.07. The yield criteria violation is also indicated in the principal stress plot through several stress states residing outside the yield surface contour for candidate material TM800s/M21. In contrast, the inclusion of appropriate stress constraints in the optimization formulation for Dsg. 3 eliminates the high-stress sharp corner in the optimized design. The corresponding YFM plot with a maximum YFM value of 1 indicates effective prevention of failure. The corresponding principal stress plots show that stress states satisfy the anisotropic Tsai–Hill and isotropic von Mises yield criteria for fiber-reinforced TM800s/M21 and corresponding isotropic candidate materials, respectively. Results imply that anisotropic stress constraints prevent high-stress localization in fiber-reinforced composites by incorporating fiber-reinforced material strength information in the optimization formulation. Effectively, the proposed framework with anisotropic stress constraints can design a

Table 3
Overview of numerical examples.

Example	Design cases	Highlights
Ex. 1	Design comparison between proposed formulation and conventional optimization approaches.	Merits of anisotropic stress constraints and isotropic material in fiber-reinforced composite optimization.
Ex. 2	Design comparison with different fiber-reinforced materials	Influence of various Tsai–Wu strength anisotropy on optimized designs.
Ex. 3	Design with domain containing crack and two load cases.	Crack removal and simultaneous stress constraining for both load cases.

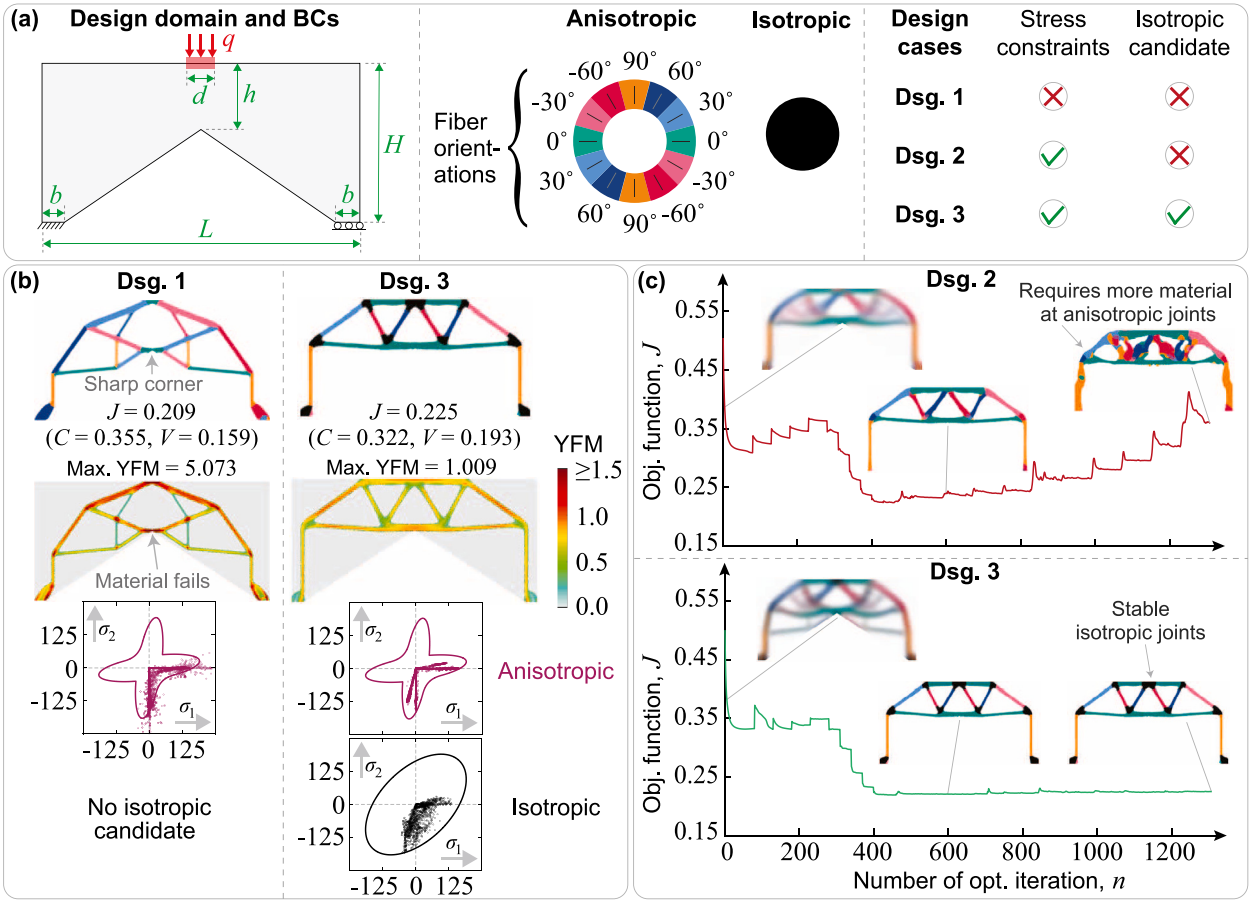

Fig. 6. Advantages of the proposed framework over other optimization approaches. (a) Design domain and boundary conditions (BCs), L = 12.00 m, H = 6.00 m, h = 2.50 m, d = 1.00 m, b = 0.55 m, $q = 4.00 \times 10^4$ kN/m, color indicators for the candidate fiber orientations of the anisotropic fiber-reinforced material TM800s/M21 and the corresponding isotropic material, and features of the three design cases to be compared. (b) Comparison of designs without stress constraints (Dsg. 1) and proposed framework (Dsg. 3), (c) Comparison of designs without candidate isotropic material (Dsg. 2) and proposed framework (Dsg. 3).

strong structure that shows higher load-carrying capacity without any local material failure.

Fig. 6(c) compares the design evolution history of Dsg. 2 and Dsg. 3 to illustrate the importance of an isotropic candidate material in stress-constrained fiber-reinforced composite design optimization. Without the isotropic candidate material, the design optimization for Dsg. 2 diverges at a later stage mainly due to (a) the disproportionately high stiffness and strength of anisotropic fiber-reinforced material along its fiber orientation compared to any other directions; (b) the lack of isotropic material as a candidate; and (c) the effect of continuation of penalization parameters. To maximize structural stiffness and strength while minimizing total volume with fiber composites, the optimized designs tend to align the fibers with the principal stress path or the load path. From this optimization perspective, the joints, where two or more load paths intersect, favor a mixing of fiber orientations (i.e., multiple orientations selected in the same element with $\bar{m}_e^{(i)} \in (0,1)$, $i = 1,\ldots,N_\theta$) over fiber orientation in any one direction to provide sufficient stiffness and strength along multiple load paths. In early iterations, the penalization effect is relatively mild because of the relaxed interpolated yield surface with $p_{f_\xi} > 1$ [70], and the optimization is more tolerant to the mixing of orientations. By contrast, the penalization of orientation mixing becomes harsher in later iterations, especially when p_{f_ξ} gradually reduces to 1. This harsher penalization of mixed orientation causes the violation of stress constraints and forces the optimizer to choose any one of the mixed fiber orientations aligned with one of the intersecting load paths. However, the overall stress also increases when mixed orientations are separated at the multi-axially loaded joints, as no isotropic material phase is available in the candidate material set to provide sufficient stiffness and strength along multiple load paths. This further amplifies stress constraint violation for Dsg. 2, and the optimizer responds by aggressively adding more material to the design, especially at the joints. As a result, the objective function for Dsg. 2 increases due to the increasing volume term, thereby causing the divergence. The diverged design of Dsg. 2 indicates that the bi- or tri-axial joints occupied with a highly anisotropic material are not suitable for design optimization with the prescribed load. In

contrast, Dsg. 3 in Fig. 6(c) shows that the inclusion of isotropic material stabilizes the design evolution. The isotropic material occupies the bi- and tri-axial joints in the optimized design, as it provides sufficient stiffness and strength along multiple directions, unlike the fiber-reinforced material. We remark that, the appearance of isotropic material at the joints is driven by the utilization of isotropic stiffness and strength at multi-axial load paths and not by volume constraint. Despite having an elastic modulus lower than the anisotropic material, the appearance of isotropic material is favored by the optimizer and is necessary to form an integrated optimized fiber-reinforced composite structure. A similar observation is found in [32], where compliance-minimization with smoothly varying fiber without dissimilar strength information also generated optimized designs with orthotropic slender members and isotropic joints.

4.2. Example 2: Effect of anisotropic strength in michell structure-like designs

The second example investigates the influence of different strength anisotropy corresponding to various fiber-reinforced materials on Michell structure-like design formations. In this example, we consider four design cases, each with one of the four different fiber-reinforced materials and corresponding different isotropic materials from Table 1. We use same compliance weight factor value $w = 0.25$ for all four design cases. Fig. 7(a) shows the design domain and BC, and color indicators for the candidate fiber orientations of the anisotropic fiber-reinforced material and the candidate isotropic material. Each of the four design cases with different candidate fiber-reinforced materials has different magnitudes of the prescribed load q because of large deviations in the four fiber-reinforced material strengths. Fig. 7(b) presents the Tsai–Wu strength parameters for the fiber-reinforced materials used in the four different design cases. Fig. 7(c) shows the optimized designs with respective YFM fringe plots and corresponding principal stress plots with anisotropic and isotropic candidate material yield surfaces for the four design cases.

The four optimized designs with different yield strength anisotropy of constituting fiber-reinforced materials show distinct topology. Although the optimized designs have similar volumes, the prescribed load carried per unit volume is maximum for Graphite/epoxy, followed by Kevlar/epoxy, TM800s/M21, and LBL, respectively, which reflects the fiber-direction strength hierarchy in those materials. The optimized design with TM800s/M21 and corresponding isotropic material has symmetric tension and compression members, as the material has a symmetric Tsai–Hill yield surface with equal tension and compression strengths both along and perpendicular to the fiber directions. The optimized design with Kevlar/epoxy and corresponding isotropic material has a longer outer-most tension member compared to its outer-most compression member, implying the structure prefers to carry the prescribed load through tension. In this case, the optimizer utilizes the higher tensile strength of the Kevlar/epoxy material to minimize the objective. The optimized design with Graphite/epoxy and corresponding isotropic material has a longer compression member despite having equal uniaxial tension and compression strengths along the fiber direction. Such asymmetric topology results from the very small tension strength of Graphite/epoxy in the direction perpendicular to the fiber, and is also reflected in the corresponding Tsai–Wu yield surface contour. The shape of the Graphite/epoxy yield surface indicates a rapid decrease in tension strength for even a small deviation of the load path from the fiber direction, which restricts the formation of tension members during the intermediate stage of the optimization when members may have mixed orientations or the anisotropic members are not completely aligned with the load path. For a similar reason, the design with laminated bamboo lumber (LBL) and corresponding isotropic material shows a longer compression path, i.e., prefers to carry the prescribed load through compression, despite having a higher uniaxial tension strength, as the tension strength of LBL reduces drastically for fiber orientations not aligned with uniaxial load paths.

Further, four optimized designs all form isotropic joints. The symmetric design with TM800s/M21 eliminates both sharp corners to prevent material failure. Asymmetric designs all eliminate the sharp corners opposite to the dominant load-carrying side. The retained corners are occupied with isotropic materials as they have higher biaxial strength compared to the respective anisotropic candidates. For each design case, the YFM fringe plots and the principal stress plots corresponding to the anisotropic and isotropic materials show respective yield criteria satisfactions, and demonstrate the capability of the proposed formulation to handle distinct fiber-reinforced and isotropic materials with respective appropriate yield strength and criteria.

4.3. Example 3: Multiple load case design

The third example extends the proposed framework to a multiple load case problem. Most real-life structures are subjected to multiple loading conditions that may act simultaneously, which entails the satisfaction of appropriate anisotropic and isotropic material strength requirements for all possible load cases. In this example, we optimize the structure simultaneously for two load cases by performing two finite element analyses and thereby including element-wise stress constraints for both load cases in each optimization iteration. Fig. 8(a) shows the design domain with a crack, boundary conditions, and the two load cases q_1 and q_2. The crack is modeled as disconnected nodes in half of the design domain by taking advantage of the symmetry, as shown in Fig. 8(a). For the candidate materials, we use the candidate fiber orientations of anisotropic fiber-reinforced material laminated bamboo lumber (LBL) and corresponding isotropic material shown in Fig. 8(a), with material properties from Table 1. We use a weight factor value $w = 0.3$ for this example.

Fig. 8(c) shows the optimized design and the YFM fringe plots corresponding to the two load cases. The optimized structure eliminates the crack tip by forming a rounded geometry to reduce stress concentration. The YFM plots show maximum YFM values as 1, indicating no stress violation for both load cases. Furthermore, the isotropic material occupies the crack tip and other joints because of multi-axial stress states in these locations, as the significantly low bi-axial strength of fiber-reinforced LBL material (see Fig. 5) is not sufficient to prevent joint failure for the prescribed loads. The fiber-reinforced material LBL occupies the slender members with nearly uniaxial stress states and fibers aligned with principal stress directions to improve the objective function by providing higher stiffness per unit volume compared to the candidate isotropic material. The example illustrates that the proposed formulation with anisotropic stress constraints can address strong geometrical singularities such as crack tips and utilize material isotropy–anisotropy for fiber-reinforced composites even with multiple load cases.

5. Conclusions

This study presents a stress-constrained multimaterial topology optimization framework to design fiber-reinforced composites composed of both anisotropic (i.e., orthotropic) and isotropic materials. We discover and demonstrate that both anisotropic and isotropic materials are needed to achieve high performance in stiffness and strength for fiber composites. The proposed method enables the full exploitation of anisotropic and isotropic material properties, i.e., stiffness and yield criteria, to design composites with optimized compliance and volume while simultaneously preventing local material failure. Such capability is realized through adopting a novel yield function interpolation scheme, which simultaneously and consistently integrates both a load factor-based Tsai–Wu yield criterion for anisotropic (i.e., orthotropic) fiber-reinforced material and a von Mises yield criterion for isotropic material, in the optimization formulation as stress constraints. The

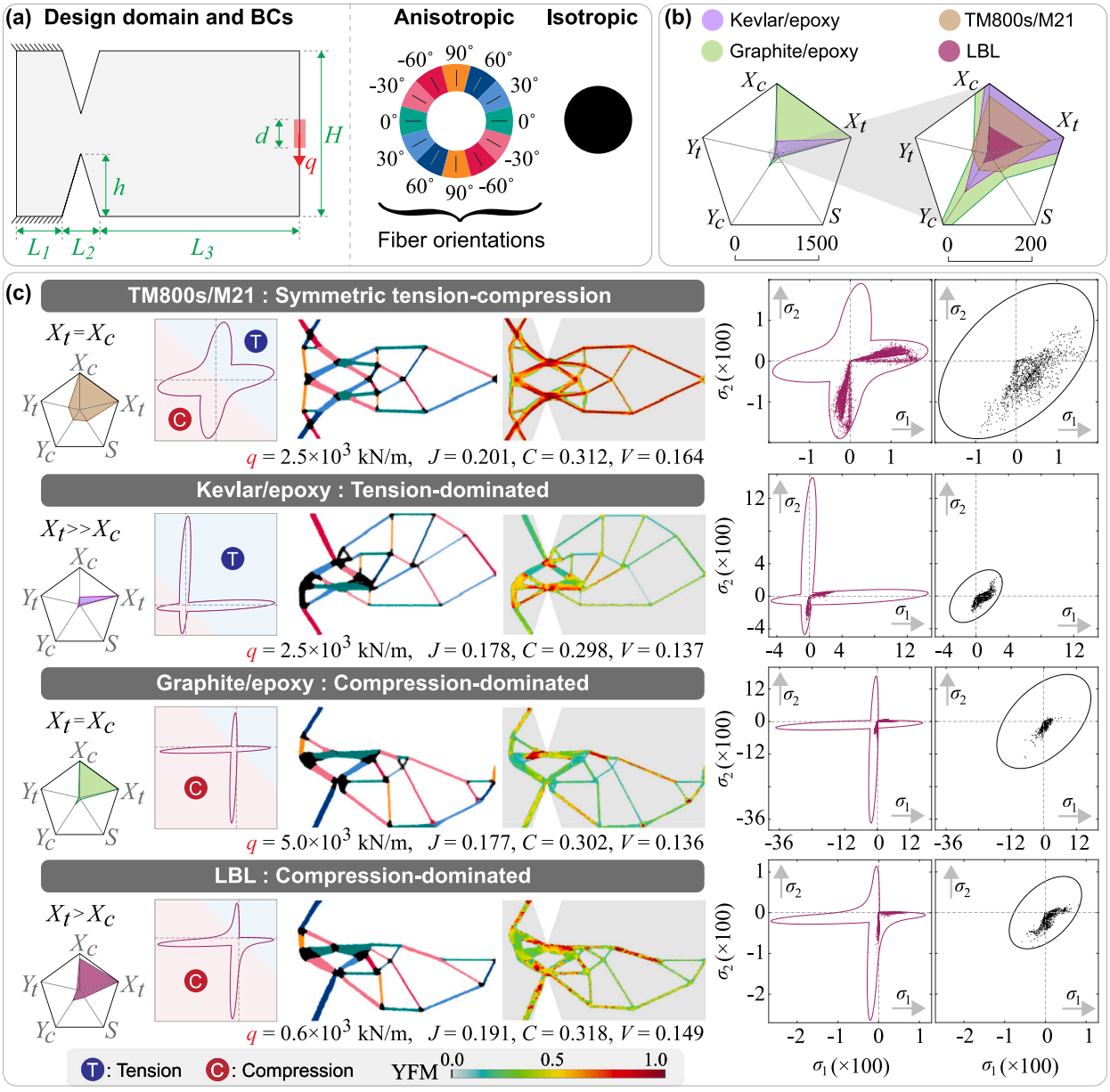

Fig. 7. Influence of different strength anisotropy extents on Michell structure-like optimized designs. (a) Design domain and BCs, $L_1 = 0.30$ m, $L_2 = 0.30$ m, $L_3 = 1.45$ m, $H = 1.20$ m, $h = 0.45$ m, $d = 0.50$ m, q varies as 2.50×10^3 kN/m, 2.50×10^3 kN/m, 5.00×10^3 kN/m, and 0.60×10^3 kN/m for TM800s/M21, Kevlar/epoxy, Graphite/epoxy, and LBL, respectively, and color indicators for the candidate fiber orientations of the anisotropic fiber-reinforced materials and the corresponding isotropic materials. (b) Radar charts showing the Tsai–Wu strength parameters of the different fiber-reinforced materials. (c) Features of anisotropic strength, corresponding optimized designs, and dissimilar yield criteria satisfaction for the four design cases with different fiber-reinforced materials.

resulting optimization formulation with many local stress constraints is effectively solved by the AL algorithm.

Using the proposed formulation, we investigate several stress-sensitive design problems to demonstrate the unique advantages of our framework in fiber-reinforced composite design. The proposed anisotropic yield function interpolation scheme enables optimized designs containing both anisotropic fiber-reinforced and isotropic materials. The results demonstrate:

- the benefit of introducing isotropic material in fiber-reinforced composites to strengthen multi-axial load paths,
- the proposed formulation effectively prevents excessive stress localization and material failure in both anisotropic and isotropic parts of the structure, thereby enhancing overall structural strength for a set of prescribed load cases,
- the capability of the proposed framework to handle fiber-reinforced materials spanning a wide range of strength anisotropy, and
- the seamless and simultaneous incorporation of multiple load cases in the optimization process.

While this study demonstrates composite designs that simultaneously contain dissimilar materials governed by anisotropic Tsai–Wu and isotropic von Mises yield criteria, we remark that candidate material phases with multiple fiber directions may be included for different objective and constraint functions that could potentially benefit from having fibers in multiple directions throughout the cross-section. In addition, the proposed methodology can be readily extended to candidate material phases with uniaxially- or multiaxially oriented fibers throughout or parts of the cross-sections. Moreover, the proposed

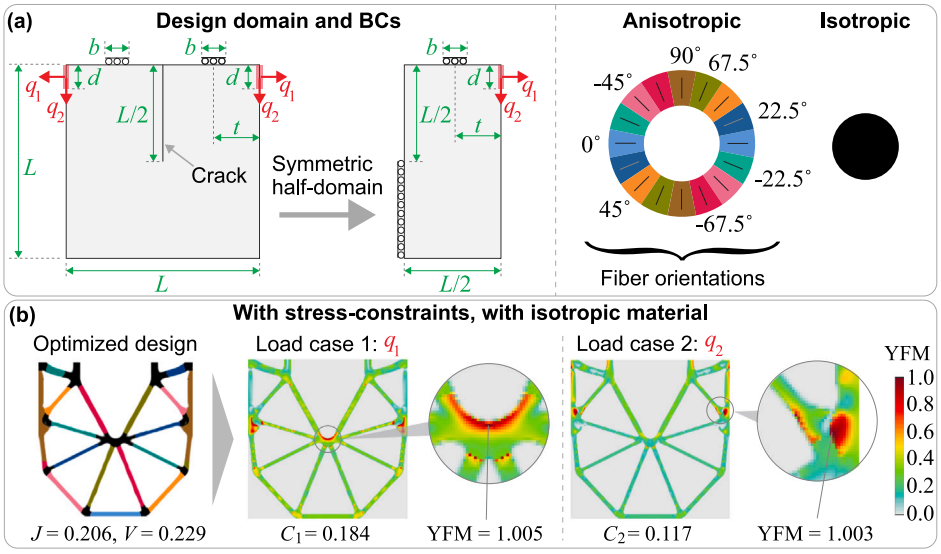

Fig. 8. Fiber-reinforced composite topology optimization with simultaneous incorporation of two load cases using the proposed framework. (a) Design domain and BCs, $L = 2.00$ m, $d = 0.10$ m, $b = 0.10$ m, $t = 0.50$ m, $q_1 = 1.40 \times 10^3$ kN/m, $q_2 = 1.68 \times 10^3$ kN/m, and color indicators for the candidate fiber orientations of the anisotropic fiber-reinforced material LBL and the corresponding isotropic material. (b) Optimized design and corresponding yield function measure (YFM) distributions for the two load cases.

design framework with the yield function interpolation scheme is sufficiently general and can be extended to include various anisotropic and isotropic yield criteria beyond Tsai–Wu and von Mises, to enhance the stiffness and strength of a diverse range of lightweight composite structures.

CRediT authorship contribution statement

Rahul Dev Kundu: Methodology, Software, Investigation, Writing – original draft, Writing – review & editing. **Xiaojia Shelly Zhang:** Conceptualization, Methodology, Investigation, Writing – original draft, Writing – review & editing, Supervision, Funding acquisition.

Declaration of competing interest

The authors declare that they have no known competing financial interests or personal relationships that could have appeared to influence the work reported in this paper.

Data availability

Data will be made available on request.

Acknowledgments

The authors would like to acknowledge the following financial supports. X.S. Zhang and R.D. Kundu were supported by the U.S. National Science Foundation (NSF) EAGER Award CMMI-2127134 and CAREER Award CMMI-2047692. The information provided in this paper is the sole opinion of the authors and does not necessarily reflect the view of the sponsoring agencies.

Appendix A. Advantage of using load factor-based Tsai–Wu yield criteria

As the optimization problem involves two types of candidate materials, i.e., anisotropic (i.e., orthotropic) fiber-reinforced material with Tsai–Wu failure criterion and isotropic material with von Mises failure criterion, it is important to impose similar penalization severity on both failure criteria violation to facilitate unbiased distribution of candidate materials during optimization. However, the original form of the Tsai–Wu failure criterion (13) imposes more severe penalty compared to the von Mises criterion (12) for same extent of stress violation when used as stress constraint. To address this problem, we use the load factor, a concept introduced in [37] to optimize fiber orientations in a composite laminate, to incorporate the Tsai–Wu yield criterion in the stress constraints. The load factor-based Tsai–Wu yield criterion has two advantages. First, the load factor-based Tsai-wu criterion becomes identical to the von Mises criterion when isotropic strength parameters are used, i.e., $X_t = X_c = Y_t = Y_c = \sqrt{3}S$, which enables consistent interpolation of the two dissimilar yield criteria. Second, the load factor represents a uniform measure of stress violation in tension and compression with respect to the origin in the principal stress plane for Tsai–Wu strength asymmetry in tension–compression. These two advantages are demonstrated using Fig. A.9 in the following.

Fig. A.9(a) compares the stress penalization of actual Tsai–Wu and load factor-based Tsai–Wu criteria with von Mises yield criterion using an isotropic material with von Mises strength $\bar{\sigma}_{\text{iso}} = 1$. As the von Mises criterion may be considered a special case of more general Tsai–Wu criterion, we express the Tsai–Wu strength parameters of this isotropic material as $X_t = X_c = Y_t = Y_c = \sqrt{3}S = \bar{\sigma}_{\text{iso}} = 1$. Notice that, for the material at yield strength limit, the yield surfaces $f^{(\text{vm})}(\boldsymbol{\sigma}) = 1$, $f^{(\text{tw})}(\boldsymbol{\sigma}) = 1$ and $\eta^{(\text{tw})}(\boldsymbol{\sigma}) = 1$ are identical. Then we consider an element in uniaxial tension with tensile stress magnitude σ_t. For this element, the principal stress components are $\{\sigma_1, \sigma_2\} = \{\sigma_t, 0\}$, and for this uniaxial tension state, the von Mises yield function takes the value 2, i.e., $(f^{(\text{vm})}(\boldsymbol{\sigma}) = 2)$, for $\sigma_1 = \sigma_t = 2$. Now we evaluate the actual and load factor-based Tsai–Wu yield criteria on this element. The actual Tsai–Wu yield function value becomes 2, i.e., $(f^{(\text{tw})}(\boldsymbol{\sigma}) = 2)$ for $\sigma_1 = \sigma_t = 1.4$, whereas, the load factor-based Tsai–Wu yield function value becomes 2, i.e., $(\eta^{(\text{tw})}(\boldsymbol{\sigma}) = 2)$ for $\sigma_1 = \sigma_t = 2$. We observe that, the actual Tsai–Wu criterion imposes equal penalty for a lower stress violation, implying more severe penalization for same stress violation, compared to the von Mises criterion. In contrast, the load factor-based Tsai–Wu criterion is identical to the von Mises criterion for isotropic strength parameters, and imposes equal penalization as the von Mises criterion.

Fig. A.9(b) compares the penalization obtained from actual Tsai–Wu and load factor-based Tsai–Wu criteria for a fiber-reinforced material with asymmetric tension–compression Tsai–Wu strength parameters, given by $X_t = 3, X_c = 1, Y_t = 1, Y_c = 1$, and $S = 1/\sqrt{3}$. For the material at yield strength limit, the yield surfaces $f^{(\text{tw})}(\boldsymbol{\sigma}) = 1$ and $\eta^{(\text{tw})}(\boldsymbol{\sigma}) = 1$ are identical. We consider an element of this material assuming fiber direction is always aligned with the direction of principal stress σ_1. To

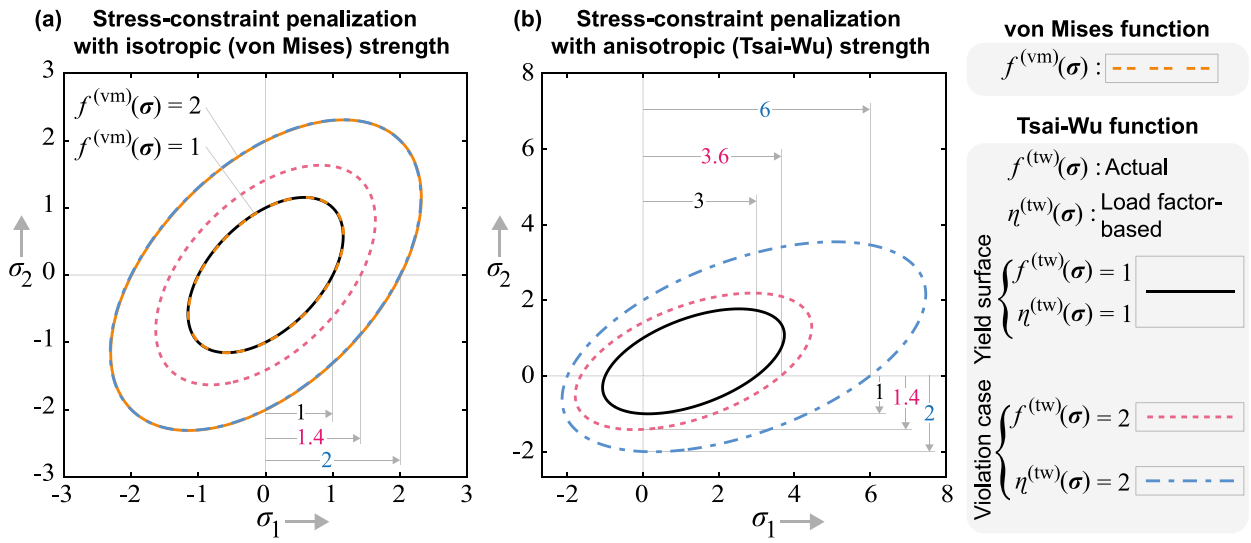

Fig. A.9. Merits of using load factor-based Tsai–Wu yield criterion over actual Tsai–Wu criterion: (a) load factor-based Tsai–Wu criterion is equivalent to traditional von Mises stress-constraint in terms of penalization severity, and (b) load factor-based Tsai–Wu uniformly penalizes tension and compression with respect to the origin.

evaluate penalization from both types of Tsai–Wu criteria in tension-dominated regions, we consider an uniaxial tension stress of magnitude σ_t for the element acting along the fiber direction. For this uniaxial tension case, the principal stress components are $\{\sigma_1, \sigma_2\} = \{\sigma_t, 0\}$. Further, we consider a separate case of uniaxial compression stress of magnitude σ_c for the element acting perpendicular to the fiber direction. For this uniaxial compression case, the principal stress components are $\{\sigma_1, \sigma_2\} = \{0, -\sigma_c\}$. For the two uniaxial stress states, the effective uniaxial strengths of the element in tension and compression become $X_t = 3$ and $Y_c = 1$, respectively. For the uniaxial tension case, the actual Tsai–Wu yield function value becomes 2 when $\sigma_1 = \sigma_t = 3.645$, i.e., the tension stress is 1.215 times the tension strength X_t, whereas, for the uniaxial compression case, the actual Tsai–Wu yield function value becomes 2 when $\sigma_2 = -\sigma_c = -1.414$, i.e., the compression stress is 1.414 times the compression strength Y_c. Clearly, we observe a disparity in tension–compression stress violation and corresponding penalization when the actual Tsai–Wu yield criterion is used in the stress constraints. However, the load factor-based Tsai–Wu yield function value becomes 2 for $\sigma_1 = \sigma_t = 6$ in the uniaxial tension case, and for $\sigma_2 = -\sigma_c = -2$ in the uniaxial compression case. In both cases, the load factor-based Tsai–Wu yield function gives same penalization for same extent of relative stress violation in tension and compression. Furthermore, we observe that the actual Tsai–Wu yield function creates concentric surfaces $f^{(\mathrm{tw})}(\boldsymbol{\sigma}) = k, k > 1$, with respect to the center of the elliptical Tsai–Wu yield surface $f^{(\mathrm{tw})}(\boldsymbol{\sigma}) = 1$, whereas, the load factor-based Tsai–Wu yield function creates concentric surfaces $\eta^{(\mathrm{tw})}(\boldsymbol{\sigma}) = k, k > 1$, with respect to the origin in the principal stress plane. Hence, the load factor serves as a proportional measure of stress violation uniform in tension and compression.

Appendix B. Sensitivity analysis

Gradient-based design updates require the sensitivity of the AL function in Eq. (19). Here, we present the detailed expression of the sensitivity for the proposed multimaterial formulation for single load case, and extending this to multiple load cases is straight-forward. The sensitivities of the AL function with respect to $\boldsymbol{\rho}$ and $\boldsymbol{\xi}^{(i)}, i = 1, \ldots, N_\xi$ are obtained through the chain rule:

$$\frac{\partial \psi^{(n)}}{\partial \rho_e} = \sum_{j=1}^{N_e} \frac{\partial \psi^{(n)}}{\partial \bar{\rho}_j} \frac{\partial \bar{\rho}_j}{\partial \tilde{\rho}_j} \frac{\partial \tilde{\rho}_j}{\partial \rho_e}, \tag{B.1}$$

$$\frac{\partial \psi^{(n)}}{\partial \xi_e^{(k)}} = \sum_{j=1}^{N_e} \frac{\partial \psi^{(n)}}{\partial \bar{\xi}_j^{(k)}} \frac{\partial \bar{\xi}_j^{(k)}}{\partial \tilde{\xi}_j^{(k)}} \frac{\partial \tilde{\xi}_j^{(k)}}{\partial \xi_e^{(k)}}, \tag{B.2}$$

The second and third terms of the R.H.S. of the Eqs. (B.1) and (B.2) can be computed based on (1) and (2), respectively. Thus, the main complication lies in the first terms. $\partial \psi^{(n)} / \partial \bar{\xi}_j^{(k)}$ is computed as

$$\frac{\partial \psi^{(n)}}{\partial \bar{\xi}_j^{(k)}} = \frac{\partial \psi^{(n)}}{\partial \bar{m}_j^{(i)}} \frac{\partial \bar{m}_j^{(i)}}{\partial \bar{\xi}_j^{(k)}}, \quad j = 1, \ldots, N_e, \tag{B.3}$$

where the sensitivity of material physical variables with respect to material Heaviside projected variables are obtained as

$$\frac{\partial \bar{m}_j^{(i)}}{\partial \bar{\xi}_j^{(k)}} = \sum_{r=1}^{2^{(N_m-1)}} b_r^{(i)} \left((-1)^{(N_m - 1 + \sum_{k=1}^{N_m-1} c_r^{(k)})} \prod_{\substack{n=1 \\ n \neq k}}^{(N_m-1)} (\bar{\xi}_e^{(n)} + c_j^{(n)} - 1) \right), \quad i = 1, \ldots, N_m - 1,$$

$$\text{and,} \frac{\partial \bar{m}_j^{(N_m)}}{\partial \bar{\xi}_j^{(k)}} = - \sum_{i=1}^{N_m-1} \frac{\partial \bar{m}_j^{(i)}}{\partial \bar{\xi}_j^{(k)}}. \tag{B.4}$$

We obtain the sensitivities of the AL function with respect to the physical variables as

$$\frac{\partial \psi^{(n)}}{\partial \bar{\rho}_e} = \frac{w}{C^*} \left(-\mathbf{U}^T \frac{\partial \mathbf{F}_{\mathrm{int}}}{\partial \bar{\rho}_e} \right) + (1 - w) \frac{v_e}{\sum_{k=1}^{N} v_k} + \frac{1}{N} \left(\left[\lambda_e^{(n)} + \mu^{(n)} h_e^{(n)} \right] \frac{\partial h_e^{(n)}}{\partial \bar{\rho}_e} + \boldsymbol{\Lambda}^T \frac{\partial \mathbf{F}_{\mathrm{int}}}{\partial \bar{\rho}_e} \right) \tag{B.5}$$

$$\frac{\partial \psi^{(n)}}{\partial \bar{m}_e^{(i)}} = \frac{w}{C^*} \left(-\mathbf{U}^T \frac{\partial \mathbf{F}_{\mathrm{int}}}{\partial \bar{m}_e^{(i)}} \right) + \frac{1}{N} \left(\left[\lambda_e^{(n)} + \mu^{(n)} h_e^{(n)} \right] \frac{\partial h_e^{(n)}}{\partial \bar{m}_e^{(i)}} + \boldsymbol{\Lambda}^T \frac{\partial \mathbf{F}_{\mathrm{int}}}{\partial \bar{m}_e^{(i)}} \right) \tag{B.6}$$

where the gradients of internal force $\mathbf{F}_{\mathrm{int}}$ with respect to the physical variables can be expressed for a linear material model using solid material stiffness matrices $\mathbf{k}_{0,e}^{(i)}$ and the displacement vector $\mathbf{u}_e$ for the e^{th} element as

$$\frac{\partial \mathbf{F}_{\mathrm{int}}}{\partial \bar{\rho}_e} = [(1 - \epsilon) p_\rho \bar{\rho}_e^{p_\rho - 1}] \left(\sum_{i=1}^{N_m} (\bar{m}_e^{(i)})^{p_{\bar{\xi}}} \mathbf{k}_{0,e}^{(i)} \right) \mathbf{u}_e, \tag{B.7}$$

$$\frac{\partial \mathbf{F}_{\mathrm{int}}}{\partial \bar{m}_e^{(i)}} = [\epsilon + (1 - \epsilon) \bar{\rho}_e^{p_\rho}] \left(p_{\bar{\xi}} (\bar{m}_e^{(i)})^{p_{\bar{\xi}} - 1} \mathbf{k}_{0,e}^{(i)} \right) \mathbf{u}_e, \tag{B.8}$$

and $\boldsymbol{\Lambda}$ is the adjoint vector obtained by solving the adjoint system

$$\mathbf{K}\boldsymbol{\Lambda} = - \sum_{e=1}^{N} \left[\lambda_e^{(n)} + \mu^{(n)} h_e^{(n)} \right] \frac{\partial h_e^{(n)}}{\partial \mathbf{U}}. \tag{B.9}$$

The gradients of equality constraints $h_e^{(n)}$ vanish when $g_e^{(n)} < -(\lambda_e^{(n)}/\mu^{(n)})$; otherwise, they are computed through (superscript n is omitted hereafter because all the operations are carried out in the same n^{th} AL step):

$$\frac{\partial h_e}{\partial \bar{\rho}_e} = \frac{\partial g_e}{\partial \bar{\rho}_e} = [(1-\epsilon)p_\rho \bar{\rho}_e^{p_\rho - 1}](f_e^{(\xi)} - 1)((f_e^{(\xi)} - 1)^2 + 1) \tag{B.10}$$

$$\frac{\partial h_e}{\partial \bar{m}_e^{(i)}} = \frac{\partial g_e}{\partial \bar{m}_e^{(i)}} = [\epsilon + (1-\epsilon)\bar{\rho}_e^{p_\rho}](3(f_e^{(\xi)} - 1)^2 + 1)\frac{\partial f_e^{(\xi)}}{\partial \bar{m}_e^{(i)}} \tag{B.11}$$

$$\frac{\partial h_e}{\partial \mathbf{U}} = \frac{\partial g_e}{\partial \mathbf{U}} = [\epsilon + (1-\epsilon)\bar{\rho}_e^{p_\rho}](3(f_e^{(\xi)} - 1)^2 + 1)\frac{\partial f_e^{(\xi)}}{\partial \mathbf{U}} \tag{B.12}$$

The gradients of $f^{(\xi)}$ with respect to the physical material variables $\bar{m}^{(i)}$ and state variable $\mathbf{U}$ are obtained for element e as

$$\frac{\partial f_e^{(\xi)}}{\partial \bar{m}_e^{(i)}} = p_{f_\xi}(\bar{m}_e^{(i)})^{p_{f_\xi}-1}\eta^{(i)}, \tag{B.13}$$

$$\frac{\partial f_e^{(\xi)}}{\partial \mathbf{U}} = \sum_{i=1}^{N_m}(\bar{m}_e^{(i)})^{p_{f_\xi}}\frac{\partial \eta^{(i)}}{\partial \mathbf{U}}, \tag{B.14}$$

$$\frac{\partial \eta^{(i)}}{\partial \mathbf{U}} = \left(\frac{\partial \eta^{(i)}}{\partial \sigma_1^{(i)}}\frac{\partial \sigma_1^{(i)}}{\partial \boldsymbol{\sigma}^{(i)}} + \frac{\partial \eta^{(i)}}{\partial \sigma_2^{(i)}}\frac{\partial \sigma_2^{(i)}}{\partial \boldsymbol{\sigma}^{(i)}} + \frac{\partial \eta^{(i)}}{\partial \sigma_6^{(i)}}\frac{\partial \sigma_6^{(i)}}{\partial \boldsymbol{\sigma}^{(i)}}\right)\cdot\frac{\partial \boldsymbol{\sigma}^{(i)}}{\partial \mathbf{U}} \tag{B.15}$$

where $\eta^{(i)}$ is the load factor-based Tsai–Wu yield function of i^{th} candidate material phase, and $\boldsymbol{\sigma}^{(i)}$ is the Cauchy stress tensor corresponding to i^{th} candidate material. Note that, the von Mises yield function is identical to the load factor-based Tsai–Wu yield function when isotropic strength parameters, i.e., $X_t = X_c = Y_t = Y_c = \sqrt{3}S = \bar{\sigma}_{\text{iso}}$ are considered for the isotropic candidate material, and hence, the gradients can be derived from same expression. The gradient of the Cauchy stress tensor with respect to displacement vector is obtained as $\frac{\partial \boldsymbol{\sigma}^{(i)}}{\partial \mathbf{U}} = \mathbf{C}^{(i)}\mathbf{B}^{(i)}$, where $\mathbf{C}^{(i)}$ is the solid material constitutive matrix and $\mathbf{B}^{(i)}$ is the strain–displacement matrix of Material i ($i = 1, \ldots, N_m$).

References

[1] Vasiliev V, Razin A. Anisogrid composite lattice structures for spacecraft and aircraft applications. Compos Struct 2006;76(1):182–9. http://dx.doi.org/10.1016/j.compstruct.2006.06.025, Fifteenth International Conference on Composite Materials, URL https://www.sciencedirect.com/science/article/pii/S0263822306002649.

[2] Bruggi M, Taliercio A. Topology optimization of the fiber-reinforcement retrofitting existing structures. Int J Solids Struct 2013;50(1):121–36. http://dx.doi.org/10.1016/j.ijsolstr.2012.09.009, URL https://www.sciencedirect.com/science/article/pii/S0020768312003927.

[3] Rupp CJ, Evgrafov A, Maute K, Dunn ML. Design of piezoelectric energy harvesting systems: A topology optimization approach based on multilayer plates and shells. J Intell Mater Syst Struct 2009;20(16):1923–39. http://dx.doi.org/10.1177/1045389X09341200.

[4] Vatanabe S, Paulino G, Silva E. Design of functionally graded piezocomposites using topology optimization and homogenization–toward effective energy harvesting materials. Comput Methods Appl Mech Engrg 2013;266:205–18. http://dx.doi.org/10.1016/j.cma.2013.07.003.

[5] Connolly F, Polygerinos P, Walsh CJ, Bertoldi K. Mechanical programming of soft actuators by varying fiber angle. Soft Robotics 2015;2(1):26–32. http://dx.doi.org/10.1089/soro.2015.0001.

[6] Connolly F, Walsh CJ, Bertoldi K. Automatic design of fiber-reinforced soft actuators for trajectory matching. Proc Natl Acad Sci 2017;114(1):51–6. http://dx.doi.org/10.1073/pnas.1615140114, arXiv:https://www.pnas.org/doi/pdf/10.1073/pnas.1615140114, URL https://www.pnas.org/doi/abs/10.1073/pnas.1615140114.

[7] Gao Y, Zhao X, Han X, Wang P, Zheng WJ. Soft actuator based on metal/hydrogel nanocomposites with anisotropic structure. Macromol Chem Phys 2022;223(3):2100117. http://dx.doi.org/10.1002/macp.202100117, arXiv:https://onlinelibrary.wiley.com/doi/pdf/10.1002/macp.202100117, URL https://onlinelibrary.wiley.com/doi/abs/10.1002/macp.202100117.

[8] Pei B, Wang W, Fan Y, Wang X, Watari F, Li X. Fiber-reinforced scaffolds in soft tissue engineering. Regen Biomater 2017;4(4):257–68. http://dx.doi.org/10.1093/rb/rbx021, arXiv:https://academic.oup.com/rb/article-pdf/4/4/257/19424679/rbx021.pdf.

[9] Nikbakt S, Kamarian S, Shakeri M. A review on optimization of composite structures Part I: Laminated composites. Compos Struct 2018;195:158–85. http://dx.doi.org/10.1016/j.compstruct.2018.03.063, URL https://www.sciencedirect.com/science/article/pii/S0263822317336279.

[10] Bendsøe MP, Sigmund O. Topology optimization: theory, methods, and applications. In: Engineering. Berlin, Germany: Springer; 2003, p. 370.

[11] Sigmund O, Maute K. Topology optimization approaches. Struct Multidiscip Optim 2013;48(6):1031–55. http://dx.doi.org/10.1007/s00158-013-0978-6.

[12] Wang C, Zhao Z, Zhou M, Sigmund O, Zhang XS. A comprehensive review of educational articles on structural and multidisciplinary optimization. Struct Multidiscip Optim 2021;64(5):2827–80. http://dx.doi.org/10.1007/s00158-021-03050-7.

[13] Zhou Y, Nomura T, Saitou K. Multi-component topology and material orientation design of composite structures (MTO-C). Comput Methods Appl Mech Engrg 2018;342:438–57. http://dx.doi.org/10.1016/j.cma.2018.07.039.

[14] Nomura T, Kawamoto A, Kondoh T, Dede EM, Lee J, Song Y, et al. Inverse design of structure and fiber orientation by means of topology optimization with tensor field variables. Composites B 2019;176:107187. http://dx.doi.org/10.1016/j.compositesb.2019.107187, URL https://www.sciencedirect.com/science/article/pii/S1359836819307218.

[15] Lee J, Kim D, Nomura T, Dede EM, Yoo J. Topology optimization for continuous and discrete orientation design of functionally graded fiber-reinforced composite structures. Compos Struct 2018;201:217–33. http://dx.doi.org/10.1016/j.compstruct.2018.06.020, URL https://www.sciencedirect.com/science/article/pii/S0263822318305798.

[16] Völkl H, Klein D, Franz M, Wartzack S. An efficient bionic topology optimization method for transversely isotropic materials. Compos Struct 2018;204:359–67. http://dx.doi.org/10.1016/j.compstruct.2018.07.079, URL https://www.sciencedirect.com/science/article/pii/S0263822317340175.

[17] da Silva ALF, Salas RA, Nelli Silva EC, Reddy J. Topology optimization of fibers orientation in hyperelastic composite material. Compos Struct 2020;231:111488. http://dx.doi.org/10.1016/j.compstruct.2019.111488, URL https://www.sciencedirect.com/science/article/pii/S0263822319306786.

[18] Luo Y, Chen W, Liu S, Li Q, Ma Y. A discrete-continuous parameterization (DCP) for concurrent optimization of structural topologies and continuous material orientations. Compos Struct 2020;236:111900. http://dx.doi.org/10.1016/j.compstruct.2020.111900, URL https://www.sciencedirect.com/science/article/pii/S0263822319331241.

[19] Zhang XS, Chi H, Zhao Z. Topology optimization of hyperelastic structures with anisotropic fiber reinforcement under large deformations. Comput Methods Appl Mech Engrg 2021;378:113496. http://dx.doi.org/10.1016/j.cma.2020.113496, URL https://www.sciencedirect.com/science/article/pii/S0045782520306812.

[20] Ding H, Xu B. A novel discrete–continuous material orientation optimization model for stiffness-based concurrent design of fiber composite. Compos Struct 2021;273:114288. http://dx.doi.org/10.1016/j.compstruct.2021.114288, URL https://www.sciencedirect.com/science/article/pii/S0263822321007509.

[21] Lu Y, Tong L. Concurrent optimization of topologies and fiber orientations for laminated composite structures. Compos Struct 2022;295:115749. http://dx.doi.org/10.1016/j.compstruct.2022.115749, URL https://www.sciencedirect.com/science/article/pii/S0263822322005256.

[22] Elvas A, Sohouli A, Suleman A. Simultaneous topology and fiber path optimization of composite structures with MAC constraints. Compos Struct 2022;294:115645. http://dx.doi.org/10.1016/j.compstruct.2022.115645, URL https://www.sciencedirect.com/science/article/pii/S0263822322004287.

[23] Jung T, Lee J, Nomura T, Dede EM. Inverse design of three-dimensional fiber reinforced composites with spatially-varying fiber size and orientation using multiscale topology optimization. Compos Struct 2022;279:114768. http://dx.doi.org/10.1016/j.compstruct.2021.114768, URL https://www.sciencedirect.com/science/article/pii/S0263822321012174.

[24] Nomura T, Dede EM, Lee J, Yamasaki S, Matsumori T, Kawamoto A, et al. General topology optimization method with continuous and discrete orientation design using isoparametric projection. Internat J Numer Methods Engrg 2015;101(8):571–605. http://dx.doi.org/10.1002/nme.4799, arXiv:https://onlinelibrary.wiley.com/doi/pdf/10.1002/nme.4799, URL https://onlinelibrary.wiley.com/doi/abs/10.1002/nme.4799.

[25] Xia Q, Shi T. Optimization of composite structures with continuous spatial variation of fiber angle through shepard interpolation. Compos Struct 2017;182:273–82. http://dx.doi.org/10.1016/j.compstruct.2017.09.052, URL https://www.sciencedirect.com/science/article/pii/S0263822317322766.

[26] Kiyono C, Silva E, Reddy J. A novel fiber optimization method based on normal distribution function with continuously varying fiber path. Compos Struct 2017;160:503–15. http://dx.doi.org/10.1016/j.compstruct.2016.10.064, URL https://www.sciencedirect.com/science/article/pii/S0263822316314957.

[27] Salas RA, Ramírez-Gil FJ, Montealegre-Rubio W, Silva ECN, Reddy J. Optimized dynamic design of laminated piezocomposite multi-entry actuators considering fiber orientation. Comput Methods Appl Mech Engrg 2018;335:223–54. http://dx.doi.org/10.1016/j.cma.2018.02.011, URL https://www.sciencedirect.com/science/article/pii/S0045782518300902.

[28] Chandrasekhar A, Kumar T, Suresh K. Build optimization of fiber-reinforced additively manufactured components. Struct Multidiscip Optim 2020;61(1):77–90. http://dx.doi.org/10.1007/s00158-019-02346-z, URL https://doi.org/10.1007/s00158-019-02346-z.

[29] Papapetrou VS, Patel C, Tamijani AY. Stiffness-based optimization framework for the topology and fiber paths of continuous fiber composites. Composites B 2020;183:107681. http://dx.doi.org/10.1016/j.compositesb.2019.107681, URL https://www.sciencedirect.com/science/article/pii/S1359836819341733.

[30] Boddeti N, Tang Y, Maute K, Rosen DW, Dunn ML. Optimal design and manufacture of variable stiffness laminated continuous fiber reinforced composites. Sci Rep 2020;10(1):16507. http://dx.doi.org/10.1038/s41598-020-73333-4, URL https://doi.org/10.1038/s41598-020-73333-4.

[31] Kim D, Lee J, Nomura T, Dede EM, Yoo J, Min S. Topology optimization of functionally graded anisotropic composite structures using homogenization design method. Comput Methods Appl Mech Engrg 2020;369:113220. http://dx.doi.org/10.1016/j.cma.2020.113220, URL https://www.sciencedirect.com/science/article/pii/S0045782520304059.

[32] Schmidt M-P, Couret L, Gout C, Pedersen CBW. Structural topology optimization with smoothly varying fiber orientations. Structural and Multidisciplinary Optimization 2020;62(6):3105–26. http://dx.doi.org/10.1007/s00158-020-02657-6.

[33] Stegmann J, Lund E. Discrete material optimization of general composite shell structures. Internat J Numer Methods Engrg 2005;62(14):2009–27. http://dx.doi.org/10.1002/nme.1259.

[34] Bruyneel M. SFP—a new parameterization based on shape functions for optimal material selection: application to conventional composite plies. Struct Multidiscip Optim 2011;43(1):17–27. http://dx.doi.org/10.1007/s00158-010-0548-0.

[35] Gao T, Zhang W, Duysinx P. A bi-value coding parameterization scheme for the discrete optimal orientation design of the composite laminate. Internat J Numer Methods Engrg 2012;91(1):98–114. http://dx.doi.org/10.1002/nme.4270.

[36] Coelho P, Guedes J, Rodrigues H. Multiscale topology optimization of bi-material laminated composite structures. Compos Struct 2015;132:495–505. http://dx.doi.org/10.1016/j.compstruct.2015.05.059, URL https://www.sciencedirect.com/science/article/pii/S0263822315004420.

[37] Groenwold AA, Haftka RT. Optimization with non-homogeneous failure criteria like Tsai–Wu for composite laminates. Struct Multidiscip Optim 2006;32(3):183–90. http://dx.doi.org/10.1007/s00158-006-0020-3.

[38] Walker M, Smith R. A technique for the multiobjective optimisation of laminated composite structures using genetic algorithms and finite element analysis. Compos Struct 2003;62(1):123–8. http://dx.doi.org/10.1016/S0263-8223(03)00098-9, URL https://www.sciencedirect.com/science/article/pii/S0263822303000989.

[39] IJsselmuiden ST, Abdalla MM, Gürdal Z. Implementation of strength-based failure criteria in the lamination parameter design space. AIAA J 2008;46(7):1826–34. http://dx.doi.org/10.2514/1.35565.

[40] Lee JW, Kim JJ, Yoon GH. Stress constraint topology optimization using layerwise theory for composite laminates. Compos Struct 2019;226:111184. http://dx.doi.org/10.1016/j.compstruct.2019.111184, URL https://www.sciencedirect.com/science/article/pii/S0263822318335724.

[41] Huang J, Haftka RT. Optimization of fiber orientations near a hole for increased load-carrying capacity of composite laminates. Struct Multidiscip Optim 2005;30(5):335–41. http://dx.doi.org/10.1007/s00158-005-0519-z.

[42] Lund E. Discrete material and thickness optimization of laminated composite structures including failure criteria. Struct Multidiscip Optim 2018;57(6):2357–75. http://dx.doi.org/10.1007/s00158-017-1866-2.

[43] Shimoda M, Muramatsu Y, Tsukihara R. Minimization of maximum failure criterion of laminated composite shell structure by optimizing distributed-material orientation. Struct Multidiscip Optim 2020;61(4):1547–71. http://dx.doi.org/10.1007/s00158-019-02435-z.

[44] Bruggi M, Milani G, Taliercio A. Design of the optimal fiber-reinforcement for masonry structures via topology optimization. Int J Solids Struct 2013;50(13):2087–106. http://dx.doi.org/10.1016/j.ijsolstr.2013.03.007, URL https://www.sciencedirect.com/science/article/pii/S002076831300108X.

[45] Mirzendehdel AM, Rankouhi B, Suresh K. Strength-based topology optimization for anisotropic parts. Addit Manuf 2018;19:104–13. http://dx.doi.org/10.1016/j.addma.2017.11.007, URL https://www.sciencedirect.com/science/article/pii/S2214860416303475.

[46] Ma G, Yang W, Wang L. Strength-constrained simultaneous optimization of topology and fiber orientation of fiber-reinforced composite structures for additive manufacturing. Adv Struct Eng 2022;25(7):1636–51. http://dx.doi.org/10.1177/13694332221088946.

[47] Eckrich M, Arrabiyeh PA, Dlugaj AM, May D. Structural topology optimization and path planning for composites manufactured by fiber placement technologies. Compos Struct 2022;289:115488. http://dx.doi.org/10.1016/j.compstruct.2022.115488, URL https://www.sciencedirect.com/science/article/pii/S0263822322002793.

[48] Guo X, Zhang W, Zhong W. Stress-related topology optimization of continuum structures involving multi-phase materials. Comput Methods Appl Mech Engrg 2014;268:632–55. http://dx.doi.org/10.1016/j.cma.2013.10.003, URL https://www.sciencedirect.com/science/article/pii/S0045782513002557.

[49] Jeong SH, Choi D-H, Yoon GH. Separable stress interpolation scheme for stress-based topology optimization with multiple homogeneous materials. Finite Elem Anal Des 2014;82:16–31. http://dx.doi.org/10.1016/j.finel.2013.12.003, URL https://www.sciencedirect.com/science/article/pii/S0168874X13002138.

[50] Chu S, Gao L, Xiao M, Luo Z, Li H. Stress-based multi-material topology optimization of compliant mechanisms. Internat J Numer Methods Engrg 2018;113(7):1021–44. http://dx.doi.org/10.1002/nme.5697, arXiv:https://onlinelibrary.wiley.com/doi/pdf/10.1002/nme.5697, URL https://onlinelibrary.wiley.com/doi/abs/10.1002/nme.5697.

[51] Xu S, Liu J, Zou B, Li Q, Ma Y. Stress constrained multi-material topology optimization with the ordered SIMP method. Comput Methods Appl Mech Engrg 2021;373:113453. http://dx.doi.org/10.1016/j.cma.2020.113453, URL https://www.sciencedirect.com/science/article/pii/S0045782520306381.

[52] Li W, Wang F, Sigmund O, Zhang XS. Design of composite structures with programmable elastic responses under finite deformations. J Mech Phys Solids 2021;151:104356. http://dx.doi.org/10.1016/j.jmps.2021.104356, URL https://www.sciencedirect.com/science/article/pii/S0022509621000533.

[53] Conde FM, Coelho PG, Guedes JM. Multi-material and strength-oriented microstructural topology optimization applied to discrete phase and functionally graded materials. Struct Multidiscip Optim 2022;65(4):127. http://dx.doi.org/10.1007/s00158-022-03209-w.

[54] Thomsen J. Topology optimization of structures composed of one or two materials. Struct Optim 1992;5(1):108–15. http://dx.doi.org/10.1007/BF01744703.

[55] Sigmund O, Torquato S. Design of materials with extreme thermal expansion using a three-phase topology optimization method. J Mech Phys Solids 1997;45(6):1037–67. http://dx.doi.org/10.1016/S0022-5096(96)00114-7.

[56] Yin L, Ananthasuresh G. Topology optimization of compliant mechanisms with multiple materials using a peak function material interpolation scheme. Struct Multidiscip Optim 2001;23(1):49–62.

[57] Zhang XS, Paulino GH, Ramos AS. Multi-material topology optimization with multiple volume constraints: a general approach applied to ground structures with material nonlinearity. Struct Multidiscip Optim 2018;57(1):161–82. http://dx.doi.org/10.1007/s00158-017-1768-3.

[58] Zhang XS, Chi H. Efficient multi-material continuum topology optimization considering hyperelasticity: Achieving local feature control through regional constraints. Mech Res Commun 2020;105:103494. http://dx.doi.org/10.1016/j.mechrescom.2020.103494, URL https://www.sciencedirect.com/science/article/pii/S0093641320300239.

[59] Zhang XS, Chi H, Paulino GH. Adaptive multi-material topology optimization with hyperelastic materials under large deformations: A virtual element approach. Comput Methods Appl Mech Engrg 2020;370:112976. http://dx.doi.org/10.1016/j.cma.2020.112976.

[60] Zhao Z, Zhang XS. Design of graded porous bone-like structures via a multi-material topology optimization approach. Struct Multidiscip Optim 2021;64(2):677–98. http://dx.doi.org/10.1007/s00158-021-02870-x.

[61] Bendsøe MP, Sigmund O. Material interpolation schemes in topology optimization. Arch Appl Mech 1999;69(9):635–54. http://dx.doi.org/10.1007/s004190050248.

[62] Sigmund O. Design of multiphysics actuators using topology optimization – Part II: Two-material structures. Comput Methods Appl Mech Engrg 2001;190(49):6605–27. http://dx.doi.org/10.1016/S0045-7825(01)00252-3.

[63] Wang F, Lazarov BS, Sigmund O. On projection methods, convergence and robust formulations in topology optimization. Struct Multidiscip Optim 2011;43(6):767–84. http://dx.doi.org/10.1007/s00158-010-0602-y.

[64] Zhao Z, Zhang XS. Topology optimization of hard-magnetic soft materials. J Mech Phys Solids 2022;158:104628. http://dx.doi.org/10.1016/j.jmps.2021.104628, URL https://www.sciencedirect.com/science/article/pii/S0022509621002684.

[65] Sigmund O. Morphology-based black and white filters for topology optimization. Struct Multidiscip Optim 2007;33(4):401–24. http://dx.doi.org/10.1007/s00158-006-0087-x.

[66] Bourdin B. Filters in topology optimization. Internat J Numer Methods Engrg 2001;50(9):2143–58. http://dx.doi.org/10.1002/nme.116.

[67] Giraldo-Londoño O, Paulino GH. A unified approach for topology optimization with local stress constraints considering various failure criteria: von Mises, Drucker–Prager, Tresca, Mohr–Coulomb, Bresler– Pister and Willam–Warnke. Proc R Soc A 2020. http://dx.doi.org/10.1098/rspa.2019.0861, 4762019086120190861.

[68] Giraldo-Londoño O, Paulino GH. PolyStress: a Matlab implementation for local stress-constrained topology optimization using the augmented Lagrangian method. Struct Multidiscip Optim 2021;63(4):2065–97. http://dx.doi.org/10.1007/s00158-020-02760-8.

[69] Zhou M, Rozvany G. The COC algorithm, Part II: Topological, geometrical and generalized shape optimization. Comput Methods Appl Mech Engrg 1991;89(1–3):309–36.

[70] Kundu RD, Li W, Zhang XS. Multimaterial stress-constrained topology optimization with multiple distinct yield criteria. Extreme Mech Lett 2022;54:101716. http://dx.doi.org/10.1016/j.eml.2022.101716, URL https://www.sciencedirect.com/science/article/pii/S2352431622000657.

[71] Mises Rv. Mechanik der festen Körper im plastisch- deformablen Zustand. Nachr Ges Wissensch Göttingen Math-Phys Kl 1913;4:582–92, URL http://eudml.org/doc/58894.

[72] Tsai SW, Wu EM. A general theory of strength for anisotropic materials. J Compos Mater 1971;5(1):58–80. http://dx.doi.org/10.1177/002199837100500106.

[73] Duysinx P, Sigmund O. New developments in handling stress constraints in optimal material distribution. In: 7th AIAA/USAF/NASA/ISSMO symposium on multidisciplinary analysis and optimization. American Institute of Aeronautics and Astronautics; 1998, http://dx.doi.org/10.2514/6.1998-4906, 0.
[74] Bertsekas DP. Nonlinear programming. Belmont, MA: Athena Scientific; 1999.
[75] Nocedal J, Wright S. Numerical optimization. New York, NY: Springer; 2006, http://dx.doi.org/10.1007/978-0-387-40065-5.
[76] Pereira J, Fancello E, Barcellos C. Topology optimization of continuum structures with material failure constraints. Struct Multidiscip Optim 2004;26(1–2):50–66.
[77] Fancello EA. Topology optimization for minimum mass design considering local failure constraints and contact boundary conditions. Struct Multidiscip Optim 2006;32(3):229–40. http://dx.doi.org/10.1007/s00158-006-0019-9.
[78] Emmendoerfer H, Fancello EA. A level set approach for topology optimization with local stress constraints. Internat J Numer Methods Engrg 2014;99(2):129–56.
[79] da Silva GA, Beck AT, Sigmund O. Stress-constrained topology optimization considering uniform manufacturing uncertainties. Comput Methods Appl Mech Engrg 2019;344:512–37. http://dx.doi.org/10.1016/j.cma.2018.10.020, URL https://www.sciencedirect.com/science/article/pii/S0045782518305231.
[80] Senhora FV, Giraldo-Londoño O, Menezes IFM, Paulino GH. Topology optimization with local stress constraints: a stress aggregation-free approach. Struct Multidiscip Optim 2020;62(4):1639–68. http://dx.doi.org/10.1007/s00158-020-02573-9.
[81] da Silva GA, Aage N, Beck AT, Sigmund O. Local versus global stress constraint strategies in topology optimization: A comparative study. Internat J Numer Methods Engrg 2021;122(21):6003–36. http://dx.doi.org/10.1002/nme.6781, URL https://onlinelibrary.wiley.com/doi/abs/10.1002/nme.6781.
[82] da Silva GA, Aage N, Beck AT, Sigmund O. Three-dimensional manufacturing tolerant topology optimization with hundreds of millions of local stress constraints. Internat J Numer Methods Engrg 2021;122(2):548–78. http://dx.doi.org/10.1002/nme.6548, URL https://onlinelibrary.wiley.com/doi/abs/10.1002/nme.6548.
[83] Svanberg K. The method of moving asymptotes—a new method for structural optimization. Internat J Numer Methods Engrg 1987;24(2):359–73. http://dx.doi.org/10.1002/nme.1620240207.